



Topological chiral currents in the Gross-Neveu model extensionE. Tirrito ¹, M. Lewenstein ^{2,3} and A. Bermudez^{4,5}¹*International School for Advanced Studies (SISSA), via Bonomea 265, 34136 Trieste, Italy*²*ICFO–Institut de Ciències Fotòniques, The Barcelona Institute of Science and Technology, Av. Carl Friedrich Gauss 3, 08860 Castelldefels (Barcelona), Spain*³*ICREA, Lluis Companys 23, 08010 Barcelona, Spain*⁴*Departamento de Física Teórica, Universidad Complutense, 28040 Madrid, Spain*⁵*Instituto de Física Teórica, UAM-CSIC, Universidad Autónoma de Madrid, Cantoblanco, 28049 Madrid, Spain*

(Received 3 February 2022; accepted 5 July 2022; published 28 July 2022)

We unveil an interesting connection of Lorentz-violating quantum field theories, studied in the context of the standard model extension, and Hubbard-type models of topological crystalline phases. These models can be interpreted as a regularization of the former and, as hereby discussed, explored with current quantum simulators based on ultracold atoms in optical Raman lattices. In particular, we present a complete analysis of the Creutz-Hubbard ladder under a generic magnetic flux, which regularizes a Gross-Neveu model extension and presents a characteristic circulating chiral current whose nonzero value arises from a specific violation of Lorentz invariance. We present a complete phase diagram with trivial insulators, ferromagnetic and antiferromagnetic phases, and current-carrying topological crystalline phases. These predictions are benchmarked using tools from condensed matter and quantum-information science, showing that self-consistent Hartree-Fock and strong-coupling Dzyaloshinskii-Moriya (D-M) methods capture the essence of the phase diagram in different regimes, which is further explored using extensive numerical simulations based on matrix-product states.

DOI: [10.1103/PhysRevB.106.045147](https://doi.org/10.1103/PhysRevB.106.045147)**I. INTRODUCTION**

The standard model (SM) of particle physics is one of the big triumphs of theoretical physics, as it provides simultaneously an accurate and economic description of nature [1]. The SM introduces a reduced set of quantum fields and, building upon elegant and simple symmetry principles, it fixes the form of their interactions and precisely accounts for all fundamental particles observed to date. However, existing difficulties in the incorporation of gravity to the SM suggest that this model could be a low-energy limit of a more fundamental theory that describes physics at a much higher scale, the Planck scale. In these theories, fundamental symmetries such as Lorentz invariance may be broken, as occurs in string theory [2] and noncommutative field theories [3]. The remnants of this *Lorentz violation* can be included in the so-called SM extension, an effective quantum field theory (QFT) in a larger parameter space that includes all possible Lorentz-violating terms with new bare couplings [4–6]. A wide variety of experiments [7], including recent quantum-information-enhanced interferometry [8], establish tight bounds on these couplings and, so far, have shown no evidence of the violation of Lorentz symmetry.

There is, however, an alternative arena where Lorentz invariance is not an exact symmetry but, instead, appears in the infrared long-wavelength limit [9]. In condensed-matter physics, many microscopic theories are formulated in terms of nonrelativistic quantum field theories [10] and, yet, Lorentz invariance and relativistic effects can appear in effective de-

scriptions of low-energy phenomena. The standard scenario where this happens is that of phase transitions [11], where the physics around some critical points can be described by Lorentz-invariant QFTs, and the renormalization group allows us to understand why Lorentz-breaking microscopic corrections become irrelevant at low energies [12,13]. Indeed, the dialogue between condensed-matter and high-energy physics has proved to be extremely fruitful in this context, see, e.g., Refs. [14–16] or [17–19]. An alternative scenario where the emergence of Lorentz invariance has turned out to be relevant is in graphene [20], Weyl semimetals [21], and topological insulators and superconductors [22].

In recent years, this fertile dialogue has broadened its scope, as Lorentz invariance has also become manifest as an effective symmetry in systems of atomic, molecular, and optical (AMO) physics [23,24]. Building upon Feynman's idea of a quantum simulator [25], there has been a number of experiments targeting Lorentz- and gauge-invariant QFTs using ultracold atoms [26–31] and trapped ions [32–34] (see, e.g., Refs. [35–39] for recent reviews). To the best of our knowledge, however, quantum simulations of Lorentz-violating extensions of the SM of particle physics have not been considered yet. Although Lorentz-breaking terms should, in fact, be the rule rather than the exception, since one starts from a nonrelativistic model that accurately describes these AMO systems, the difficulty lies in tailoring those systems so the Lorentz-violating terms that survive in the long-wavelength limit correspond precisely to those considered in the standard model extension (SME) [4]. This may change the role of the

SME, which has routinely provided a framework for some of the most precise null experiments to date [40]. Instead, if successful, AMO quantum simulators have the potential to turn the SME into a framework of experimentally testable analog physics beyond the SM. In this paper, we follow this route for a particular case, unveiling interesting connections between Lorentz-violating quantum field theories and lattice models of correlated topological phases of matter that display a persistent chiral current. We show that the latter provides a lattice regularization of a specific matter sector of the SME including, in addition, four-Fermi Gross-Neveu (GN)-type interactions. Moreover, we also discuss how these models can be implemented in experiments of ultracold atoms with synthetic spin-orbit coupling [41,42].

This paper is organized as follows: In Sec. II, we start by reviewing the physics of Hubbard ladders, which are the minimal fermionic lattice models that allow for the effect of external (background) gauge fluxes and may support a circulating, so-called chiral current. This sets the stage to introduce a particular lattice regularization of low-dimensional Lorentz-violating QFTs, the *cross-link Creutz-Hubbard ladder* for generic magnetic flux θ . We argue that this model can host a current-carrying topological crystalline phase (TCP), which is simultaneously described by a nonzero topological invariant and a circulating chiral current. A short summary of the main results of this work is then presented. In Sec. III, we explicitly construct the continuum limit of this ladder and show that it corresponds to a *Gross-Neveu model extension* (GNME) with a particular Lorentz violation that has been explored in the SME. This gives a neat perspective on the appearance of the persistent chiral current, which coexists with a nonzero topological invariant and can be used to chart the phase diagram via the associated susceptibility, as discussed in Sec. IV. In Sec. V, using a self-consistent mean-field approach analog to a large- N limit of the GN model, we study how this chiral current can be used to characterize the robustness of the TCP as the strength of the four-Fermi interactions are increased and discuss the full phase diagram of the model. We benchmark the mean-field predictions using tools developed by the condensed-matter and quantum-information communities, i.e., tensor-network variational techniques based on matrix-product states (MPSs). As discussed in the text, these quasiexact numerics confirm qualitatively the mean-field prediction of the phase diagram and correct the typical shortcomings of mean-field treatments. Finally, in Sec. VI, we present a proposal for a potential experimental realization with spin-orbit-coupled ultracold atoms. In this way, models of high-energy physics considered in the context of the SME could be accessed with table-top experiments of nonrelativistic neutral atoms at ultralow temperatures.

II. THE CREUTZ-HUBBARD LADDER WITH ARBITRARY FLUX

In this section, we describe the model under study: the cross-linked Creutz-Hubbard ladder under an arbitrary magnetic flux. Let us start, however, by reviewing briefly the context of strongly correlated behavior in ladder compounds, which has a long and fruitful history in condensed matter.

A. Previous studies on Hubbard ladders

In ladder models, the particles are arranged on a lattice composed of N_ℓ chains with N_s sites each. Typically, these particles have nearest-neighbor couplings along the vertical and horizontal directions resembling a rectangular ladder structure of N_ℓ legs [see Fig. 1(a)]. These systems interpolate between 1D and 2D as one increases the numbers of legs $N_\ell \rightarrow N_s$ and, sometimes, can host unexpected phenomena. For instance, in the context of Heisenberg ladders and their connection to the high- T_c cuprates [43], the parity of the number of legs determines the gapped/gapless nature of the model [44,45], drawing a neat connection to the Haldane conjecture of spin chains and the interplay of topology and constrained QFTs [46,47]. Through an analog of the superexchange mechanism [48], these Heisenberg ladders can be seen as the strong-coupling limit of a half-filled Hubbard ladder, where electrons interact via a strong local density-density coupling, the so-called Hubbard interaction [49]. Being quasi-1D, ladders yield a neat playground to generalize analytical methods [50–53] developed for one-dimensional systems [54]. Moreover, Hubbard and Heisenberg ladders can be explored numerically [55,56] using efficient and very accurate numerical schemes [57,58].

Getting closer to the subject of the present paper, we note that the rectangular ladders are the minimal lattice structures that can be pierced by an external magnetic flux and have a well-defined thermodynamic limit [see Figs. 1(b)–1(d)]. By increasing the number of legs, these ladders yield a clear route toward the integer [59] and fractional [60] quantum Hall effects. For the two-leg ladder, the presence of a magnetic flux modifies the fermion tunneling in a Hubbard ladder via the so-called Peierls' substitution [61] depicted in Fig. 1(b). This in turn leads to a rich phase diagram that contains Luttinger and Luther-Emery phases [62], depending on the magnetic flux and the specific filling factor. In the case of spinless fermions, on-site Hubbard interactions must be exchanged for nearest-neighbor ones [see Fig. 1(d)], the interplay of which with the magnetic flux can also give rise to various strongly correlated effects. While in the absence of the magnetic field, these finite-range interactions typically stabilize charge- and bond-density wave patterns depending on the particular filling, the situation becomes much richer as the magnetic field is switched on. For instance, one may find staggered flux phases with a pattern of local currents along the vertical and horizontal links, encompassing alternating circulations (i.e., vortices) in the plaquettes [63,64]. Moreover, one can also find kinks/antikinks that interpolate between the two possible symmetry-broken patterns of vortices, each of which hosts fractionally charged excitations in analogy to fractionalization phenomena in QFTs [65] and polymers [66,67].

The remarkable progress of ultracold atoms in optical lattices has stimulated renewed interest in the physics of the bosonic counterparts of these ladders [see Fig. 1(c)]. In particular, recent experiments [68,69] have realized a Bose-Hubbard model [70,71] in a two-leg ladder under an external magnetic flux. As discussed in previous theoretical works [72], this bosonic model can host liquid phases analogous to the Meissner and vortex phases of superconductors. These states of matter can be distinguished by a *circulating chiral current*, which has actually been measured in experiments

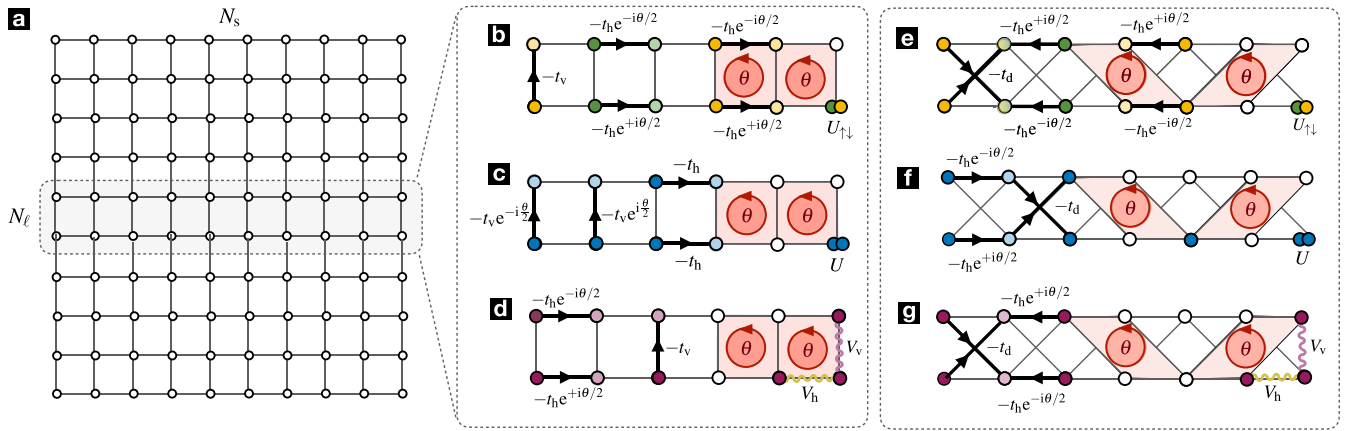


FIG. 1. Hubbard ladders pierced by a magnetic field. (a) Diagram of N_ℓ -leg ladder with open boundary conditions. Particles move across the ladder hopping along horizontal and vertical links that join the different lattice sites. (b) Rectangular two-leg ladder for spin-full fermions subjected to an external magnetic flux θ . The fermions can hop along the legs and rungs with strength $t_h e^{\pm i\theta/2}$ and t_v , respectively, and interact through a repulsive local Hubbard interaction $U_{\uparrow\downarrow}$ depending on the spin. (c) Rectangular ladder for spinless bosons subjected to an external homogeneous magnetic field. The tunneling strengths are arranged similarly to (b), and U represents the interaction strength when two bosons meet at the same lattice site. Exploiting the gauge freedom, one can arrange the Peierls' phases in the tunnelings along the vertical directions maintaining the same flux, such that the bosons pick an Aharonov-Bohm phase proportional to the flux θ when tunneling across a plaquette. (d) Rectangular ladder for spinless fermions subjected to an external magnetic flux θ , here depicted through an anticlockwise directed circle. The one-site Hubbard interaction is forbidden by Pauli exclusion, and only nearest neighbors V_v and V_h can contribute. (e)–(g) Same as (b)–(d) but for a cross-linked, so-called Creutz-Hubbard ladder. Here, the tunneling between neighboring chains occurs diagonally instead of vertically $t_v \rightarrow t_d$, forming a crossed-linked pattern. In this case, particles hopping along two possible trapezoidal plaquettes gain an Aharonov-Bohm phase proportional to the magnetic flux θ .

[68]. This current quantifies a boson flow with a natural connection to the edge states and skipping orbits of quantum Hall samples as the number of legs is increased [73]. However, as the microscopic particles are bosons, the nature of the phases differs, and one can find unique Meissner- and vortex-type ground states. In the Meissner phase, the bosonic chiral current plays the role of the screening current in superconductors (i.e., it flows in a different direction so as to screen the external magnetic flux). Alternatively, in the vortex phase, currents run along the ladder rungs, leading to vortices where the magnetic flux is not fully screened, which draws a clear analogy to type-II superconductors. More recently, this distinction has also been identified as one increases the Hubbard interactions, where one finds Meissner and vortex-type Mott insulators [74,75], as well as the so-called vortex lattices [76,77]. Let us also remark that the chiral current can also be used to unveil a quantitative connection of these quasi-1D ladders, both bosonic and fermionic, with the topologically-ordered phases [78] of the fractional quantum Hall effect [79,80].

Once the relevant literature on fermionic and bosonic Hubbard models on rectangular ladders has been reviewed, let us describe the literature on *cross-linked Hubbard ladders*. In this case, the particles can tunnel between neighboring chains, forming a crossed-linked pattern, as depicted in Figs. 1(e)–1(g). This ladder geometry was discussed by Creutz [81,82] in the context of domain-wall fermions [83–86] in lattice gauge theories [87,88]. The presence of the external magnetic field changes considerably the band structure, and can even lead to completely flat bands in the π -flux regime [89], yielding an instance of Aharonov-Bohm cages [90] with fermions locked to the plaquettes due to destructive interference [81]. In fact, this so-called Creutz ladder is an archetype of flat-band

physics [89]. In addition to these localized bulk states, there are additional edge states exponentially localized to the left- and rightmost boundaries of the ladder. These states can be understood as lower-dimensional versions [81] of domain-wall fermions [83], and correspond to the edge states of a topological insulator [22] in the symmetry class AIII/BDI [91,92]. The persistence of these topological features at finite temperatures [93,94] and adiabatic [95] or sudden [96] dynamical quenches has also been discussed in the literature. Moreover, the Creutz ladder also yields a neat scenario to explore the phenomenon of topological charge pumping [97].

Let us now briefly review some recent works exploring the strongly correlated physics of this cross-linked ladder in the presence of Hubbard-type interactions. As occurred for the rectangular ladder, there has been recent interest in studying the phases of a Bose-Hubbard model in this cross-linked geometry [see Fig. 1(f)]. Here, a flat-band-induced frustration can change the standard condensation of bosons [98] and lead to new phases of matter even for weak interactions. Depending on the filling per site, the contact interactions can lead to valence bond crystals, quasisuperfluids of paired bosons, or supersolids that arise from bound pairs of domain walls that interpolate between two valence-bond orderings [99,100]. We note that, in addition to the cold-atom quantum simulators, the bosonic Creutz-Hubbard ladder has also been discussed in the context of microwave photons in superconducting circuits [101], photonic waveguide arrays [102], and superradiant tight-binding lattices in momentum space [103]. Moving on to the spinful fermionic case of Fig. 1(e), this model yields a neat playground to understand correlation effects in topological phases of matter [104]. For instance, for attractive interactions and in the context of flat-band superconductivity

[105,106], one can find an exact Bardeen-Cooper-Schrieffer (BCS) ground state and emerging SU(2) symmetries [107]. In this case, a crossover between such BCS superconductor and a superfluid of tightly bound pairs for attractive Hubbard interactions has also been found [108,109]. The competition of BCS pairing and repulsive Hubbard interactions was discussed in Ref. [110] and shown to yield an interesting phase diagram with topological superconductors characterised by Majorana edge states. The interplay of flat-band interactions and disorder has also been explored for the fermionic Creutz-Hubbard ladder [111,112] in connection to many-body localization [113].

The inclusion of various hyperfine states in cold-atom gases in optical lattices opens another perspective for quantum simulations, as one may use the internal states as a synthetic dimension [114–116], as recently demonstrated in quantum simulators of quantum Hall ladders [117–119] or of spin-orbit coupled interacting wires [120–122]. In this context, the s -wave scattering that gives rise to SU(N) Hubbard models [123,124], can be understood as nonlocal interactions along the synthetic dimension of a rectangular ladder [see Figs. 1(b)–1(d)], giving rise to a family of models with a rich interplay between interaction-induced strong correlations and flux-induced kinetic frustration [80,125–130]. As discussed in Ref. [131], the synthetic ladders are not restricted to rectangular geometries, as one can exploit Floquet-engineering techniques [132] to induce cross-link tunnelings, giving rise to the subject of this paper: the *synthetic Creutz-Hubbard ladder*, which we now describe.

B. The synthetic Creutz-Hubbard ladder

We consider a system of spinless fermions that can be created (annihilated) at the sites of a two-leg ladder by the operators $c_{i,\ell}^\dagger$ ($c_{i,\ell}$), which are labeled by $i \in \{1, \dots, N_s\}$ and $\ell \in \{u, d\}$. The cross-link geometry of the ladder, as displayed in Fig. 1(g), is determined by the tunneling terms of the lattice Hamiltonian,

$$H_C = - \sum_{i,\ell} \left(t_h e^{-i \frac{s_\ell \theta}{2}} c_{i+1,\ell}^\dagger c_{i,\ell} + t_d c_{i+1,\ell}^\dagger c_{i,\bar{\ell}} - \frac{s_\ell \Delta \epsilon}{2} c_{i,\ell}^\dagger c_{i,\ell} + \text{H.c.} \right), \quad (1)$$

where we have introduced the horizontal (diagonal) tunneling strength t_h (t_d), the energy imbalance $\Delta \epsilon$, and the notation $s_\ell = \{+1, -1\}$ and $\bar{\ell} = \{d, u\}$ for $\ell = \{u, d\}$, respectively. Finally, we note that the complex Peierls phases of the tunnelings lead to a nonzero Aharonov-Bohm phase θ when the fermions tunnel across the trapezoidal plaquettes depicted in Fig. 1(g). Accordingly, the parameter θ can be understood as the magnetic flux Φ_B of a background magnetic field $\mathbf{B}_{bg} = \nabla \times \mathbf{A}_{bg}$ that is directed perpendicularly to the plaquette S , $\theta \in \frac{e}{\hbar} \oint_{\gamma} \mathbf{d}\mathbf{l} \cdot \mathbf{A}_{bg} = 2\pi \frac{e}{\hbar} \int_S \mathbf{dS} \cdot \mathbf{B}_{bg} = 2\pi \Phi_B / \Phi_0$, expressed in units of the flux quantum $\Phi_0 = e/h$.

As advanced in the previous section, the $\theta = \pi$ -flux limit is obtained when half a flux quantum pierces each plaquette $\Phi_B = \Phi_0/2$, the tunnelings have equal strengths $t_h = t_d$, and

the imbalance vanishes $\Delta \epsilon = 0$. This leads to an Aharonov-Bohm destructive interference and a pair of flat bands $\epsilon_{\pm}(k) = \pm 2t_h$, such that particle or hole excitations do not propagate $v_g = \partial_k \epsilon_{\pm}(k) = 0$, where $k \in \text{BZ} = [-\pi/a, \pi/a)$ is the quasimomentum of the reciprocal lattice for lattice spacing a . Moreover, these flat bands are topological, as they can be characterised by a nonzero topological invariant $\gamma_{\pm} = \mp \pi$ [131], the so-called Zak's phase $\gamma_{\pm} = \int_{\text{BZ}} dk \mathcal{A}_{\pm}(k)$ [133], where we have introduced the Berry connection $\mathcal{A}_{\pm}(k) = \langle \epsilon_{\pm}(k) | i \partial_k | \epsilon_{\pm}(k) \rangle$ [134]. As discussed in Ref. [131], the Berry connection in this π -flux limit is actually homogeneous $\mathcal{A}_{\pm}(k) = \mp 1/2$ which, in higher dimensions, would lead to a vanishing Berry curvature and one would speak of a topological flat-band structure. Let us also note that, by switching the energy imbalance $\Delta \epsilon \neq 0$, the bands (connection) will no longer be flat (homogeneous), but the topological invariant remains quantized for $|\Delta \epsilon| \leq 4t_h$. According to the underlying symmetries [135,136], this imbalanced Creutz ladder hosts an **AIII** topological insulator.

The interplay of topology and interactions can lead to exotic phases of matter in topological flat-band systems [137]. In the context of synthetic dimensions in the cold-atom scheme [131], as discussed in more detail in Sec. VI, the upper and lower legs of the ladder actually correspond to two different hyperfine states of the ground-state manifold. Therefore, a contact Hubbard interaction due to the s -wave scattering of the ultracold atoms can be interpreted as a nearest-neighbor interaction along the vertical direction connecting the legs of the synthetic ladder [see Fig. 1(g)]. This leads to the following quartic term:

$$H_{CH} = H_C + \frac{V_v}{2} \sum_{i,\ell} c_{i,\bar{\ell}}^\dagger c_{i,\ell}^\dagger c_{i,\ell} c_{i,\bar{\ell}}, \quad (2)$$

where $V_v > 0$ represents a repulsive interaction strength. As shown in Ref. [131] using various analytical and numerical techniques, the noninteracting **AIII** topological insulator is adiabatically connected to a *correlated topological insulator* in a wide lobe of parameter space $(V_v, \Delta \epsilon)$, the tip of which corresponds to $(V_v, \Delta \epsilon) = (8t_h, 0)$. This symmetry-protected topological phase is surrounded by a correlated trivial band insulator and an orbital ferromagnet. This symmetry-broken phase is characterized by the magnetic order parameter $M_y = \langle T_i^y \rangle \neq 0$, where $T_i^y = i(c_{i,d}^\dagger c_{i,u} - c_{i,u}^\dagger c_{i,d})/2$ can be understood as a spin-1/2 operator when the upper and lower leg components are interpreted as the two spin projections.

Interestingly, this π -flux regime has a direct connection to a Wilson-type discretization [138] of the GN model [139], a QFT of self-interacting fermions in (1 + 1) dimensions that shares some features with higher-dimensional non-Abelian gauge theories [88]. The GN model belongs to the family of four-Fermi field theories, originally introduced in the context of nuclear interactions by Enrico Fermi [140,141]. Specifically, it can be understood as a low-dimensional version of Nambu-Jona-Lasinio (NJL) models [15,16], and allows to explore chiral symmetry breaking by dynamical mass generation and asymptotic freedom in a renormalizable framework [139]. As discussed in Refs. [142,143], the π -flux synthetic Creutz-Hubbard ladder can be unitarily mapped onto a Wilson-type discretization of the GN model, which is described by the

following lattice Hamiltonian:

$$H_{\text{GNW}} = a \sum_{x \in \Lambda_s} \left[\left(-\bar{\Psi}(x) \left(\frac{i\gamma^1}{2a} + \frac{1}{2a} \right) \Psi(x+a) + \bar{\Psi}(x) \left(\frac{m}{2} + \frac{1}{2a} \right) \Psi(x) + \text{H.c.} \right) - \frac{g^2}{2N} (\bar{\Psi}(x) \Psi(x))^2 \right], \quad (3)$$

where $\Psi(x) = (\psi_1(x), \dots, \psi_N(x))^t$ contains N flavors of the two-component Dirac spinors $\psi_n(x)$, $\bar{\Psi}(x) = \Psi(x)^\dagger \gamma^0$ is the adjoint, and γ^0, γ^1 are the gamma matrices in a $(1+1)$ -dimensional space-time $\{\gamma^\mu, \gamma^\nu\} = 2g^{\mu\nu}$, where $g^{\mu\nu} = \text{diag}(1, -1)$ is the flat Minkowski metric. For the synthetic Creutz-Hubbard ladder Eqs. (1) and (2), one needs to set $N = 1$, $\psi_1(x) = \frac{1}{\sqrt{a}} \sin(\pi j/2) (c_{j,u}, c_{j,d})^t$ with $x = ja \in \Lambda_s$, and chose the gamma matrices $\gamma^0 = \sigma^z$, and $\gamma^1 = i\sigma^y$. The correspondence between the microscopic parameters is

$$\theta = \pi, \quad t_d = t_h, \quad ma = \frac{\Delta\epsilon}{4t_h} - 1, \quad \frac{g^2}{2N} = \frac{V_v}{4t_h}, \quad (4)$$

and the topological insulator lies in the BDI class. We note that digital quantum simulations of the GN model, including other discretizations such as the staggered-fermion approach, have also been discussed recently [144–146].

This connection yields interesting insights. On the one hand, it shows that the pseudoscalar condensate $\Pi_0 = \langle \bar{\Psi}(x) i\gamma^5 \Psi(x) \rangle$, where $\gamma^5 = \gamma^0 \gamma^1 = \sigma^x$, corresponds exactly to the order parameter of the aforementioned orbital ferromagnet $\Pi_0 \leftrightarrow M_y$. This condensate acquires a nonzero value in the parity-breaking Aoki phase [147] and also plays a role in lattice discretization of quantum chromodynamics [148, 149]. Accordingly, the numerical results of Ref. [142] show that the existence of the Aoki phase, typically predicted in the basis of a large- N expansion [147], actually survives down to the ultimate quantum limit of $N = 1$. Moreover, from the perspective of the phase diagram of the Creutz-Hubbard ladder, this Aoki phase is not an artifact of the lattice scaffolding of the continuum fields but rather a physical phase that delimits the correlated BDI topological insulator. On the other hand, the connection between these two models also shows that the standard continuum limit, where one recovers the continuum GN field theory [139], $a \rightarrow 0$ and $g^2 \rightarrow 0$, is actually the critical region separating the trivial and correlated topological insulators, and that it can be used to understand the strongly coupled features of the topological phase diagram [143].

As can be seen in Eqs. (4), however, the connection to the GN field theory and the interplay of topological phases and lattice discretizations Eq. (3) only apply to the π -flux regime of the synthetic Creutz-Hubbard ladder. It thus remains open to (i) explore the full phase diagram of the model Eqs. (1) and (2) for arbitrary magnetic flux θ , (ii) find experimentally-accessible observables to characterise it, and (iii) unveil its connection to phenomena discussed in a high-energy context. In this paper, we pursue this threefold goal and find the results summarized in the following subsection.

C. Summary of the results

We have found that the Creutz-Hubbard ladder for arbitrary magnetic flux θ Eqs. (1) and (2) has interesting connections between correlated topological phases of matter and Lorentz-

violating QFTs in the SME. Interestingly, both the topological invariant that characterizes these phases and the coupling strength of the Lorentz-violating terms, can be controlled by modifying the value of the magnetic flux that pierces the ladder. As discussed in Sec. III, in the absence of interactions and for a particular set of bare microscopic couplings, the band structure of the model describes a semimetal with a single Fermi point at momentum $k_+ = \pi/2a$ or, otherwise, at $k_- = -\pi/2a$. The dispersion relation has a different propagation speed for right- and left-moving excitations, which clearly breaks the emergent Lorentz invariance that appeared in the π -flux model [131]. Remarkably, we find that this Lorentz-breaking mechanism corresponds to a particular Lorentz violation of the SME, which also breaks parity and time-reversal symmetry [4]. In combination with Hubbard interactions, we show that the continuum limit is described by a Lorentz-violating GN model with four-Fermi terms that couple the Dirac spinors around each of these two Fermi points. We refer to this continuum limit as a GNME.

In Sec. IV, we discuss how the Lorentz violation in the GNME brings in a new feature. Whereas the π -flux Creutz-Hubbard ladder cannot support persistent currents in the groundstate, the breaking of Lorentz invariance due to the asymmetry in the speed of left- and right-moving particles can be responsible for a net current. In particular, in the non-interacting limit, we show that the ground states can simultaneously display a nonzero topological invariant and a large chiral current circulating around the ladder, both of which are consistent with inversion symmetry. Using the susceptibility associated to this chiral current, we chart the phase diagram of the model and identify wide regions of parameter space with a current-carrying topological crystalline ground state. In the limit of very strong Hubbard interactions, the half-filled ladder is described by an effective spin model that corresponds to the XY model with Dzyaloshinskii-Moriya (D-M) superexchange and subjected to a transverse field. Depending on the value of the magnetic flux, one can either find ferromagnetic or antiferromagnetic phases and second-order phase transitions that separate them from a disorder paramagnet (PM) that is preferred for sufficiently-large transverse fields.

In Sec. V, we show that the TCPs with a nonzero Zak's phase disappear in favor of these magnetic phases for sufficiently strong interactions. As a visual aid for the following discussions, we present a qualitative sketch of the phase diagram containing the various results in Fig. 2. In the parameter regime $\Delta\epsilon/4t_h \in (-1, 1)$ and $\theta \in (-\pi, \pi)$, we find that the Creutz-Hubbard ladder displays four distinct phases: a PM, a ferromagnet (FM_y), an antiferromagnet (AFM_x), and a TCP. By using a mean-field reasoning in the effective GNME of the continuum limit, we understand how the effect of interactions contributes to various mass terms for the effective Dirac fermions, which provides a qualitative understanding of the fate of the topological phases when the four-Fermi interactions are increased. We make this discussion quantitative by

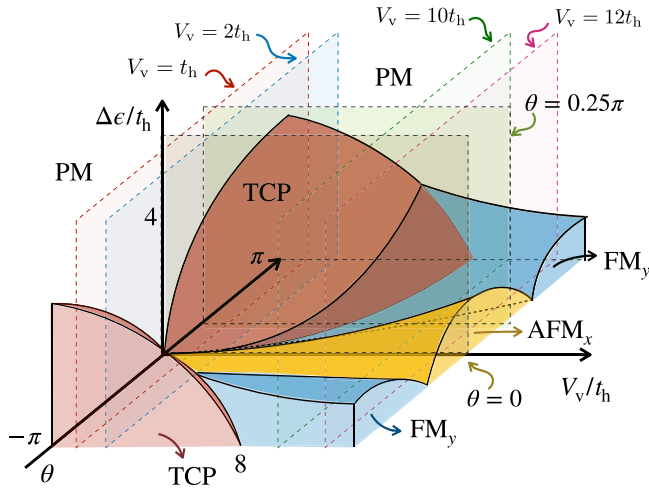


FIG. 2. Schematic phase diagram for arbitrary fluxes. Qualitative phase diagram of the Creutz-Hubbard ladder as a function of the Hubbard interactions V_v , the energy imbalance $\Delta\epsilon$, and the magnetic flux θ . At $|\theta| = \pi$, the topological phase in red is protected by a sublattice symmetry and belongs to the AIII class of topological insulators, which is surrounded by a topologically trivial paramagnet (PM) in white and a symmetry-breaking ferromagnet (FM_y) in blue, and delimited by second-order critical lines. For $|\theta| \lesssim \pi$, the sublattice symmetry is broken, and the topological phase is instead protected by inversion symmetry, representing a topological crystalline phase (TCP) which, in contrast to the π -flux limit, supports a large circulating chiral current. As the magnetic flux is decreased further toward $\theta \approx 0$, the TCP phase is also surrounded by a new symmetry-broken phase, an antiferromagnet (AFM_x) in yellow. We also depict shaded planes in parameter space where detailed numerical results are presented in the main text.

finding the mean-field parameters self-consistently, and exploring the full phase diagram in detail. Although the specific critical lines are not accurate, we show that the structure of the phase diagram predicted by this self-consistent mean field agrees with that obtained from a quasiexact density matrix renormalization group (DMRG) method. For weak interactions $V_v \ll t_h$, we show that the system has two topological lobes in parameter space ($V_v, \theta, \Delta\epsilon$). This topological phase is protected by inversion symmetry and can thus be identified with a correlated TCP that is surrounded by a trivial band insulator or by a symmetry-broken phase with ferromagnetic (antiferromagnetic) long-range order for large (small) fluxes $|\theta| \approx \pi$ ($\theta \approx 0$). Within these two lobes, the chiral current has a large absolute value and, despite the Lorentz-invariance breaking, the topological invariant remains to be nonzero $\gamma = \pm\pi$. The topological nature of this correlated phase is further confirmed by showing a twofold degeneracy of the entanglement spectrum, as calculated with our DMRG numerics. As one increases the interactions, the topological lobes become smaller and there is a SSB process where the crystalline topological phase disappears in favor of the magnetic phases. Finally, for $V_v \gg t_h$, we show that the DMRG results agree very well with those obtained from the effective spin model with anisotropic XY couplings and a Dzyaloshinskii-Moriya superexchange.

An important aspect of the current paper is that this interplay of topological phenomena, persistent chiral currents, and correlations in regularized Lorentz-violating QFTs can be realized in experiments of ultracold atoms in optical lattices. We show that by modifying recent schemes of synthetic spin-orbit coupling using Raman optical lattices, one can realize the Creutz-Hubbard ladder with an arbitrary flux, the latter being tunable by adjusting the propagation direction and the frequency of the Raman beams. This scheme avoids the use of state-dependent optical lattices or Floquet-assisted tunnelings in interacting Fermi gases, in this way minimizing the effective heating due to residual photon scattering from the auxiliary excited states. In light of recent experimental progress with Raman optical lattices [150–153], we believe that the current scheme opens another direction in the realization of strongly coupled QFTs that incorporate Lorentz-violating terms of the SME, such as the GNME studied in this paper. Additionally, the particular lattice regularization explored in this paper would allow exploration of the interplay of these relativistic models with current-carrying topological phases.

III. THE GROSS-NEVEU MODEL EXTENSION IN THE CONTINUUM LIMIT

We start by discussing the continuum limit of the Creutz-Hubbard ladder Eqs. (1) and (2) for arbitrary flux $\theta \in (-\pi, \pi]$. In the rest of this paper, we will set $t_d = t_h$ and consider half-filling conditions. One can diagonalize the noninteracting part Eq. (1) by a Fourier transform $c_{j,\ell} = \sum_{k \in \text{BZ}} e^{ikaj} c_{k,\ell} / \sqrt{N_s}$, which yields

$$H_C = \sum_{k \in \text{BZ}} \sum_{\ell, \ell'} c_{k,\ell}^\dagger h_{\ell\ell'}(k) c_{k,\ell'}, \quad h_{\ell\ell'}(k) = \epsilon_0(k) \mathbb{I}_2 + \mathbf{d}(k) \cdot \boldsymbol{\sigma}, \quad (5)$$

where we have introduced the scalar and vector functions

$$\epsilon_0(k) = -2t_h \cos\left(\frac{\theta}{2}\right) \cos(ka),$$

$$\mathbf{d}(k) = 2t_d \cos(ka) \mathbf{e}_x + \left(\frac{\Delta\epsilon}{2} - 2t_h \sin\left(\frac{\theta}{2}\right) \sin(ka)\right) \mathbf{e}_z, \quad (6)$$

and $\boldsymbol{\sigma} = \sigma^x \mathbf{e}_x + \sigma^y \mathbf{e}_y + \sigma^z \mathbf{e}_z$. Accordingly, the band structure is determined by diagonalizing the corresponding matrix, which yields the following two bands:

$$\epsilon_{\pm}(k) = \epsilon_0(k) \pm |\mathbf{d}(k)|. \quad (7)$$

In the $\theta = \pi$ -flux regime, and setting $\Delta\epsilon = 4t_h$ ($\Delta\epsilon = -4t_h$), the band structure describes a semimetal with a single Fermi point at $k_+ = +\pi/2a$ ($k_- = -\pi/2a$). As one modifies the flux $\theta \neq \pi$ and, simultaneously, adjusts the imbalance to $\Delta\epsilon = \pm 4t_h \sin(\theta/2)$, the band structure still contains the single Fermi points at the same points of the Brillouin zone [see Figs. 3(a) and 3(b)]. Since the low-energy properties are controlled by particle/hole excitations around those Fermi points, the continuum limit is obtained by a long-wavelength approximation around them, where we define a spinor field

$$\psi(x) = \frac{1}{\sqrt{a}} (c_{j,u}, c_{j,d})^t \approx e^{ik_+a} \Psi_+(x) + e^{-ik_-a} \Psi_-(x), \quad (8)$$

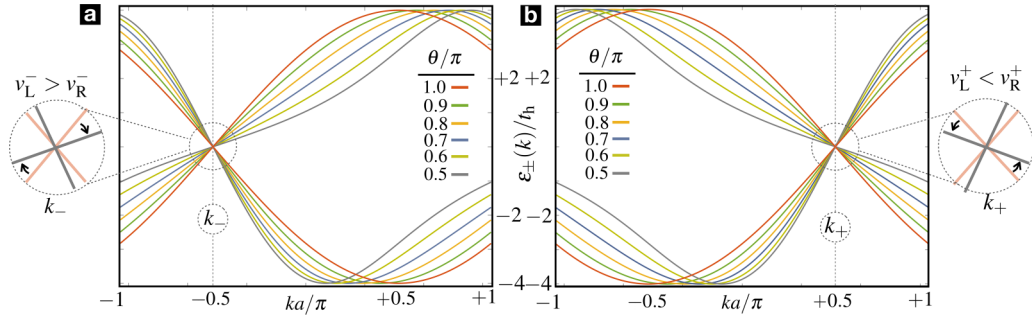


FIG. 3. Band structure and Lorentz-violating Fermi points. Dispersion relations $\epsilon_{\pm}(k)$ Eq. (7) for the two bands of the imbalanced Creutz ladder for different fluxes $\theta \in [\pi/2, \pi]$ (see the coloring labels of the insets). (a) The flux is set such that $\Delta\epsilon = -4t_h \sin(\theta/2)$, and one can see that the low-energy properties are controlled by a massless Dirac fermion at $k_- = -\pi/2a$. (b) The flux is set such that $\Delta\epsilon = 4t_h \sin(\theta/2)$, and one can see that the low-energy properties are controlled by the massless Dirac fermion at $k_+ = \pi/2a$. The left- and rightmost insets show that the corresponding Dirac cones have different propagation speeds for right- and left-moving excitations, which read v_{R}^{\pm} and v_{L}^{\pm} .

and separate the rapidly oscillating parts $e^{ik_{\eta}a}$ from the slowly varying operators $\Psi_{\eta}(x)$ for each of these Fermi points $\eta \in \{+, -\}$. These operators satisfy the desired anti-commutation relations in the continuum limit $a \rightarrow 0$, where $\{\Psi_{\eta,\ell}(x), \Psi_{\eta',\ell'}^{\dagger}(x')\} = \delta_{\eta,\eta'}\delta_{\ell,\ell'}\delta_{j,j'}/a \rightarrow \delta_{\eta,\eta'}\delta_{\ell,\ell'}\delta(x-x')$.

To obtain the QFT that governs this continuum limit, we use Eq. (8) and perform a gradient expansion for the fields $\Psi_{\eta}(x \pm a) = \Psi_{\eta}(x) \pm a\partial_x\Psi_{\eta}(x) + \mathcal{O}(a^2)$ to find the following lowest-order expressions:

$$\begin{aligned} \psi^{\dagger}(x)\hat{O}(\psi(x+a) + \psi(x-a)) &\approx 2ia \sum_{\eta} \eta \Psi_{\eta}^{\dagger}(x)\hat{O}\partial_x\Psi_{\eta}(x), \\ \psi^{\dagger}(x)\hat{O}(\psi(x+a) - \psi(x-a)) &\approx 2i \sum_{\eta} \eta \Psi_{\eta}^{\dagger}(x)\hat{O}\Psi_{\eta}(x), \end{aligned} \quad (9)$$

for any operator \hat{O} acting on the spinor degrees of freedom. Using these expressions, together with Eq. (8) and introducing the Hubbard interactions, we find that the continuum limit of the Creutz-Hubbard ladder Eqs. (1) and (2) can be expressed as

$$\begin{aligned} H_{\text{CH}} = \int dx &\left(\sum_{\eta} \bar{\Psi}_{\eta}(x)(-i(c\gamma_{\eta}^1 + \tilde{c}_{\eta}\gamma_{\eta}^0)\partial_x + m_{\eta}c^2)\Psi_{\eta}(x) \right) \\ &- \int dx \frac{g^2}{2} \left(\sum_{\eta} \bar{\Psi}_{\eta}(x)\Psi_{\eta}(x) + (-1)^{\frac{\eta}{2}} \bar{\Psi}_{\eta}(x)\Psi_{\eta}(x) \right)^2. \end{aligned} \quad (10)$$

The first line of this equation can be interpreted as the Hamiltonian QFT of a massive Dirac field for each of the species $\eta \in \{+, -\}$. These correspond to the so-called fermion doublers in the context of lattice gauge theories, which always yield an even number of species in the continuum limit [154,155]. The corresponding gamma matrices are

$$\gamma_{\pm}^0 = \sigma^z, \quad \gamma_{\pm}^1 = \pm i\sigma^y, \quad \gamma_{\pm}^5 = \pm \sigma^x, \quad (11)$$

which shows that the continuum limit around each doubler carries an opposite chirality. The effective speed of light and mass of the Dirac fermions reads

$$c = 2t_h a, \quad m_{\pm}c^2 = \frac{\Delta\epsilon}{2} \mp 2t_h \sin\left(\frac{\theta}{2}\right). \quad (12)$$

As customary in a Wilson-type discretization [138], the masses of the fermion doublers are no longer equal. This effect is not specific to the generic flux, as it also occurs in the π -flux model [131], where it underlies the existence of topological phases of matter. The result in Eqs. (12) shows that one can achieve different Wilson masses for any flux $\theta \neq 0$, and that we can use the external flux to tune their relative values. In Fig. 3(a), we see that when the flux is set such that $\Delta\epsilon = -4t_h \sin(\theta/2)$, only the Dirac fermion at k_- remains massless, which agrees with the predictions in Eqs. (12). On the other hand, for $\Delta\epsilon = +4t_h \sin(\theta/2)$, it is the massless Dirac fermion at k_+ which controls the low-energy properties as depicted in Fig. 3(b), which again agrees with Eqs. (12). Note that to use the natural units typical of relativistic quantum field theories, one must set $t_h = 1/2a$ above.

As one departs from the π -flux regime, a new term appears in the continuum limit Eq. (10) with the new coupling constant:

$$\tilde{c}_{\pm} = \pm 2t_h a \cos\left(\frac{\theta}{2}\right). \quad (13)$$

This coupling introduces an explicit violation of Lorentz symmetry, which actually corresponds to a specific term in the SME [4]. Before discussing the origin and consequences of this new term, let us comment on the second line of Eq. (10), which contains the coupling

$$\frac{g^2}{2} = \frac{V_v a}{2} = \frac{V_v}{4t_h}, \quad (14)$$

and is consistent with Eqs. (4) in the single-flavor limit $N = 1$. We can see in Eq. (10) that this interaction term introduces, in addition to four-Fermi terms for the separate species, mixing terms due to the back- and Umklapp scattering that connect the two Fermi points of the original band structure. The appearance of these terms is standard in other 1D models at half filling [54]. We note that these interaction-induced couplings between the two doublers play a key role in determining the renormalization-group flows of the microscopic parameters, which can be used to understand the shape of the phase diagram at $\theta = \pi$ [143]. We thus expect an analogous behavior for generic fluxes, albeit leading to more complicated flow equations and a richer phase diagram.

TABLE I. Parameters and observables. The correspondence between parameters and observables for the lattice Creutz-Hubbard model in Eq. (2) and its continuum limit, the fermion-doubled Gross-Neveu model, defined in Eq. (15).

Parameters and observables	
Creutz-Hubbard model	Gross-Neveu model
$V_v/4t_h$	$g^2/2$
$2t_h a$	c
$\Delta\epsilon/2 \mp 2t_h \sin(\theta/2)$	$m_{\pm} c^2$
$\pm \cos(\theta/2)$	$c_{\pm}^{\mu\nu}$
$\langle \bar{\Psi}(x) i \gamma^5 \Psi(x) \rangle$	M_y
$\langle \bar{\Psi}(x) \Psi(x) \rangle$	Δn

Summarizing, we see that besides the new term Eq. (13), the continuum limit of the synthetic Creutz-Hubbard ladder for arbitrary flux corresponds to a fermion-doubled GN model, albeit with microscopic couplings that depend on the external flux θ (the correspondence between the parameters and the observables of these two models is shown in Table I). It turns out, however, that this additional term Eq. (13) changes the physics considerably, allowing us to explore some sectors of the SME. To unveil this connection, let us find the corresponding action $S_{\text{CH}} = \int d^2x (\sum_{\eta} \Pi_{\eta} \partial_0 \Psi_{\eta} - H_{\text{CH}})$, where the canonical momenta for each of the species are $\Pi_{\eta}(x) = ic \bar{\Psi}_{\eta}(x) \gamma_{\eta}^0$ and lead to

$$S_{\text{CH}} = \int d^2x \left(\sum_{\eta} \bar{\Psi}_{\eta}(x) (ic \Gamma_{\eta}^{\mu} \partial_{\mu} - m_{\eta} c^2) \Psi_{\eta}(x) \right) + \int d^2x \frac{g^2}{2} \left(\sum_{\eta} \bar{\Psi}_{\eta}(x) \Psi_{\eta}(x) + (-1)^{\frac{x}{a}} \bar{\Psi}_{\eta}(x) \Psi_{\bar{\eta}}(x) \right)^2, \quad (15)$$

where we use Einstein's summation convention for repeated space-time indices $\mu, \nu, \tau \in \{0, 1\}$ and have introduced the modified gamma matrices for each of the doublers:

$$\Gamma_{\eta}^{\mu} = \gamma_{\eta}^{\mu} + c_{\eta}^{\mu\nu} g_{\mu\tau} \gamma_{\eta}^{\tau}. \quad (16)$$

In the context of the SME, $c^{\mu\nu}$ is a traceless tensor that contains the dominant corrections to the collisions of unpolarized electrons and positrons due to the violation of Lorentz invariance [6]. As discussed in the Introduction, these terms may arise as an effective microscopic coupling from more fundamental theories at the Planck scale, such as string theory and noncommutative QFTs [2,3]. It is remarkable that these terms arise naturally in the long-wavelength limit of the ladder. In the present context, we get one of these terms $c_{\eta}^{\mu\nu}$ for each doubler species $\eta \in \{+, -\}$ as a direct consequence of the $\theta \neq \pm\pi$ flux of the regularization Eq. (1). In fact, we find that

$$c_{\pm}^{\mu\nu} = \begin{cases} \pm \cos(\frac{\theta}{2}) & \text{if } \mu = 1, \nu = 0 \\ 0 & \text{else,} \end{cases} \quad (17)$$

which becomes nonzero away from the π -flux regime, such that $\Gamma_{\eta}^0 = \gamma_{\eta}^0$, and $\Gamma_{\eta}^1 = \gamma_{\eta}^1 + \eta \cos(\frac{\theta}{2}) \gamma_{\eta}^0$. We note that, be-

sides breaking Lorentz invariance, this term also breaks parity and time-reversal symmetry, although CPT is conserved [6]. As advanced previously, we refer to this continuum limit as a particular type of GNME.

A neat picture of the Lorentz violation caused by this term can be obtained by inspecting the band structure of Eq. (7) for generic fluxes, as depicted in Figs. 3(a) and 3(b). As already discussed in the previous section, when setting $\Delta\epsilon = \pm 4t_h \sin(\theta/2)$, one obtains a semi-metal with a Fermi point at $k_{\pm} = \pm\pi/2a$. A closer inspection of the bands [see the left- and rightmost insets of Figs. 3(a) and 3(b)] shows that the corresponding Dirac cone has a different propagation speed for right- and left-moving excitations, which reads as follows:

$$v_{\text{R}}^{\pm} = 2t_h a \left(1 \pm \cos\left(\frac{\theta}{2}\right) \right), \quad v_{\text{L}}^{\pm} = 2t_h a \left(1 \mp \cos\left(\frac{\theta}{2}\right) \right). \quad (18)$$

This clearly breaks Lorentz invariance, as $\Delta\epsilon = \pm 4t_h \sin(\theta/2)$ implies that the corresponding mass Eqs. (12) vanishes, and the fermion should thus be traveling at the same speed c Eqs. (12) in both directions, regardless of the velocity of the frame of an inertial observer. However, for nonzero $c_{\eta}^{\mu\nu}$, inertial observers moving to the right or left will see the particle traveling at different speeds, such that Lorentz symmetry is broken.

This velocity difference suggests that there might be nonzero currents in the ground state, as particles move faster in one direction than in the other. As shown below, when the ladder has periodic boundary conditions, this flow of particles corresponds to a persistent chiral current that circulates in a specific direction set by the sign of the magnetic flux. For open boundary conditions, the persistent chiral current attains a fixed nonzero value at the bulk of the ladder and gets attenuated as one approaches the left and right boundaries. Moreover, as also discussed below, this chiral current can be used to probe the full phase diagram.

IV. CHIRAL CURRENTS AND CRITICAL PHENOMENA

As discussed previously, the specific type of Lorentz violation that controls the low-energy properties Eq. (15) of the model predicts a different propagation speed for right- and left-moving particles Eqs. (18). In the underlying lattice discretization, this can yield a net *circulating chiral current* across the ladder:

$$J_c = \sum_j \left(it_h e^{i\frac{\theta}{2}} c_{j+1,u}^{\dagger} c_{j,u} - it_h e^{-i\frac{\theta}{2}} c_{j+1,d}^{\dagger} c_{j,d} + \text{H.c.} \right). \quad (19)$$

This current measures the difference of the right- and leftward fermion flows in the upper and lower legs of the ladder $J_c = J_u^{\rightarrow} - J_d^{\leftarrow}$, where J_u^{\rightarrow} and J_d^{\leftarrow} are defined as

$$J_u^{\rightarrow} = \sum_j \left(it_h e^{i\frac{\theta}{2}} c_{j+1,u}^{\dagger} c_{j,u} + \text{H.c.} \right), \quad (20)$$

$$J_d^{\leftarrow} = \sum_j \left(-it_h e^{-i\frac{\theta}{2}} c_{j+1,d}^{\dagger} c_{j,d} + \text{H.c.} \right).$$

This gives rise to a sense of circulation/chirality (i.e., $\langle J_c \rangle > 0$ clockwise circulation and $\langle J_c \rangle < 0$ anticlockwise) that

connects naturally with the current-carrying edge states of the quantum Hall effect as one increases the number of legs [73].

To avoid possible confusion, let us note that this circulating chiral current is not related to the axial current of continuum QFTs [1], which is also referred to as the chiral current, and is the Noether current associated to axial rotations. Note that for $N = 1$ [142], the four-Fermi term of the extended GN model Eq. (3) can be rewritten as

$$\frac{g^2}{2} (\bar{\Psi}(x)\Psi(x))^2 = \frac{g^2}{4} ((\bar{\Psi}(x)\Psi(x))^2 - (\bar{\Psi}(x)\gamma^5\Psi(x))^2), \quad (21)$$

such that the lattice model Eq. (3) including the Lorentz-violating term becomes invariant under continuous axial rotations $\Psi(x) \mapsto e^{i\alpha\gamma^5}\Psi(x)$, $\forall \alpha \in \mathbb{R}$. In the continuum limit, the Noether current associated to this symmetry is the aforementioned axial current $j_A^\mu = \bar{\Psi}(x)\gamma^5\gamma^\mu\Psi(x)$, which has a conserved axial charge given by

$$Q_A = \int dx j_A^0 = \int dx \bar{\Psi}(x)\gamma^5\gamma^0\Psi(x). \quad (22)$$

If we calculate the continuum limit of the circulating chiral current Eq. (19) using the fermion bilinear expressions of Eqs. (9), we find that the leading-order contribution is

$$J_c = 2t_h \cos\left(\frac{\theta}{2}\right) \int dx \bar{\Psi}(x)\Psi(x) + \mathcal{O}(a), \quad (23)$$

which clearly differs from Q_A . We see that away from the π -flux regime where the above expression Eq. (23) vanishes, the expectation value of the chiral current is proportional to the so-called scalar condensate $\Sigma_0 = \langle \bar{\Psi}(x)\Psi(x) \rangle$, the value of which marks the chiral symmetry breaking by the dynamical mass generation of the standard GN model [139]. Therefore, this circulating current cannot be directly related to the axial current or to the chiral anomaly due to a background gauge field [156,157]. In spite of this difference, given the transparent interpretation of two chiral windings, namely, the anticlockwise and clockwise circulations, it is customary to refer to this current as the chiral current.

In the following subsections, we will identify the phase diagram of the model in the noninteracting regime and the strong coupling limit. In particular, in Sec. IV A, we will characterize the phase of the model for $V_v = 0$ using the circulating chiral current and its associated susceptibility, combined with the values of the topological invariant. Instead, in Sec. IV B we will present a strongly coupled effective theory ($V_v \gg t_h$) of the model to chart its full phase diagram.

A. Chiral flows and topological phase transitions

Using the Hellmann-Feynman theorem, the expectation value of the chiral current can be expressed as the corresponding derivative of the total ground-state energy:

$$\langle J_c \rangle = 2 \left\langle \frac{\partial H_{CH}}{\partial \theta} \right\rangle = 2 \frac{\partial E_{gs}}{\partial \theta}. \quad (24)$$

This quantity contains useful information about the phase diagram, which can already be seen at the non-interacting level. In this case, $E_{gs} = \frac{a}{2\pi} \int_{BZ} dk \epsilon_-(k)$ is obtained by filling

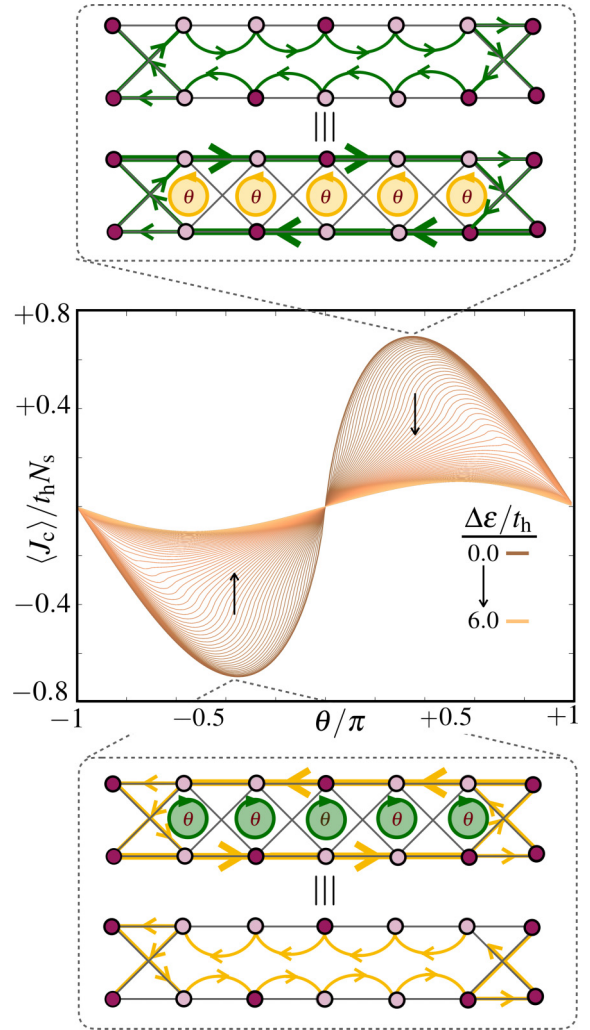


FIG. 4. Chiral current in the synthetic Creutz ladder. The main central panel presents the chiral current as a function of the magnetic flux for different imbalances $\Delta\epsilon$, using a coloring scheme that is specified in the index. In the upper and lower panels, we depict the particle flow clockwise (counterclockwise) $\langle J_c \rangle > 0$ ($\langle J_c \rangle < 0$) for positive (negative) flux $\theta > 0$ ($\theta < 0$), and also draw the analog of the skipping orbits for fermions in a quantum Hall sample.

the N_s lowest energy states of Eq. (7), yielding

$$\langle J_c \rangle = -2t_h \cos\left(\frac{\theta}{2}\right) \int_{-\pi}^{\pi} \frac{dq}{2\pi} \frac{\frac{\Delta\epsilon}{2} \sin q - 2t_h \sin\left(\frac{\theta}{2}\right) \sin^2 q}{\left|d\left(\frac{q}{a}\right)\right|}, \quad (25)$$

where we have introduced $q = ka$. Additionally, we shall also be interested in the chiral susceptibility

$$\chi_c = \left\langle \frac{\partial J_c}{\partial \theta} \right\rangle = 2 \left\langle \frac{\partial^2 H_{CH}}{\partial \theta^2} \right\rangle = 2 \frac{\partial^2 E_{gs}}{\partial \theta^2} = \frac{\partial \langle J_c \rangle}{\partial \theta}, \quad (26)$$

which can be thus obtained by taking derivatives of the above integral Eq. (25) with respect to the flux.

In the main panel of Fig. 4, we represent the dependence of the chiral current with the magnetic flux for various positive values of the imbalance $\Delta\epsilon > 0$. We observe the characteristic behavior of a screening current, as also found in fermionic [64] and bosonic [72] rectangular ladders: the particles flow

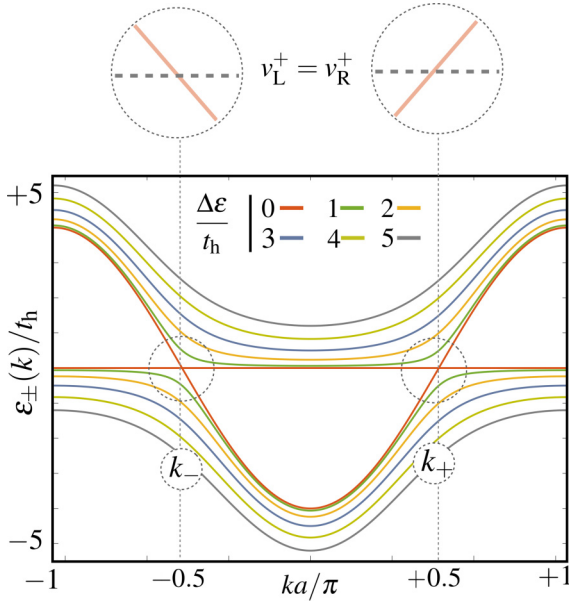


FIG. 5. Bands for the Creutz ladder for vanishing flux. Dispersion bands of the imbalanced Creutz ladder for $\theta = 0$ for different imbalance $\Delta\epsilon$, with a coloring specified in the inset. For $\theta = 0$ and $\Delta\epsilon = 0$ (red solid line), the band structure contains a flat and cosine-type band in which the two Fermi points have equal velocities $v_R^+ = v_L^-$ for right- and left-moving excitations.

clockwise (counterclockwise) $\langle J_c \rangle > 0$ ($\langle J_c \rangle < 0$) for positive (negative) flux $\theta > 0$ ($\theta < 0$) and, if charged, would thus induce a magnetic field that tends to screen the external one. In the bosonic case, this connects to the Meissner effect of a superfluid, while in the fermionic case it mimics the skipping orbits and edge states in quantum Hall samples (see the upper and lower insets of Fig. 4). This is consistent with the difference in the velocities of right- and left-moving particles v_R^+ , v_L^+ in Eqs. (18), which control the low-energy dynamics in the vicinity of $\Delta\epsilon = 4t_h \sin(\theta/2)$, which is the relevant case for the positive imbalances displayed in the figure.

We also see in this figure that the chiral flow stops at the time-reversal symmetric points $\theta \in \{-\pi, 0, \pi\}$, which is again consistent with both right- and left-moving excitations traveling at the same speed. Note that for a vanishing flux $\theta = 0$, the band structure Eq. (7) for $\Delta\epsilon = 0$ contains a flat and a cosine-type band, such that one has to consider the two Fermi points with equal velocities $v_R^+ = v_L^-$ for the right- and left-moving excitations (see Fig. 5). The low-energy theory, in this case, is thus not given by Eq. (15) with Eq. (17) for $\theta = 0$, but rather by the standard Lorentz-invariant Luttinger liquid for a cosine band, which displays no circulating currents [54]. Accordingly, in both cases $\theta \in \{-\pi, 0, \pi\}$, there is no chiral current and we recover the effective Lorentz symmetry.

For the rectangular Hubbard ladders, the circulating chiral current has a different behavior. Its dependence with the flux displays a cusplike behavior that marks the onset of a Lifshitz transition where the number of Fermi points changes [62,64]. Moreover, as one modifies the filling, the chiral current shows a linear dependence prior to the Lifshitz transition that can be used to extract information about an underlying ladder version of the Laughlin state in fractional quantum Hall phases

[79,80]. Although we do not find this exact phenomenology for the cross-linked ladder, the chiral current still carries information about phase transitions, albeit of a different nature. To see these effects, we now study the dependence of the chiral susceptibility with the magnetic flux. It turns out that the chiral susceptibility shows a clear divergence as $N_s \rightarrow \infty$ that coincides with the values of the imbalance $\Delta\epsilon = \pm 4t_h \sin(\theta/2)$, where the masses of the Dirac fermions Eqs. (12) vanish. This divergence shall thus mark the onset of a gap closure and a second-order phase transition instead of the aforementioned Lifshitz one.

In Figs. 6(a) and 6(b), we show the contour plots of the chiral current and the chiral susceptibility, respectively, as a function of $(\theta/\pi, \Delta\epsilon/t_h)$. The chiral current shows much larger absolute values within the two lobes [see Fig. 6(a)], and the maxima of the susceptibility serves to delimit the lobes and mark the phase transition [see Fig. 6(a)].

To better understand the nature of this phase transition, we now discuss the values of the Zak phase [133] for arbitrary magnetic fluxes. This topological invariant, briefly discussed in the Introduction, serves to characterize the topological phases of the Creutz ladder in the π -flux regime [131]. For generic fluxes, we find that the additional term $\epsilon_0(k)$ breaking particle-hole symmetry does not contribute to the Berry connection, such that

$$\gamma_{\pm} = \mp \int_{\text{BZ}} dk \frac{\mathbf{e}_y \cdot (\mathbf{d}(k) \times \partial_k \mathbf{d}(k))}{2|\mathbf{d}(k)|^2} \quad (27)$$

only depends on the Brillouin-zone vector field $\mathbf{d}(k)$ introduced in Eqs. (6). We note that the contribution of the Berry connection to this topological invariant is actually concentrated around the two Fermi points $k_{\pm} = \pm\pi/2a$ around which we performed the long-wavelength approximation Eq. (10). This allows us to calculate the integrals analytically, yielding

$$\gamma_{\pm} = \mp \frac{\pi}{2} \sum_{\eta=\pm} \eta \text{sgn} \left(\frac{\Delta\epsilon}{2} - \eta 2t_h \sin \left(\frac{\theta}{2} \right) \right), \quad (28)$$

which is the difference of the signs of the two fermion masses in Eqs. [(12), $\gamma_{\pm} = \pm \frac{\pi}{2} (\text{sgn}(m_-) - \text{sgn}(m_+))$]. This expression is analogous to the results found for higher-dimensional domain-wall fermions [85] and leads to the following critical lines that separate topological from trivial band insulators in the half-filled ladder:

$$\gamma_- = \begin{cases} 0, & \text{if } \Delta\epsilon > 4t_h |\sin(\frac{\theta}{2})| \\ \pi, & \text{if } 0 < \Delta\epsilon < 4t_h |\sin(\frac{\theta}{2})| \\ -\pi, & \text{if } 0 > \Delta\epsilon > -4t_h |\sin(\frac{\theta}{2})| \\ 0, & \text{if } \Delta\epsilon < -4t_h |\sin(\frac{\theta}{2})|. \end{cases} \quad (29)$$

Our results show that, in spite of our departure from the π -flux limit, and the associated breaking of Lorentz-invariance Eq. (16) and (17), one can still find a topological phase with a quantised nonzero Zak's phase in certain regions of parameter space.

This phase hosts edge states localized to the left/right boundaries of the ladder. In the π -flux limit [131], where the single-particle Hamiltonian Eq. (5) belongs to the AIII class $\{h(k), \sigma^y\} = 0$, the edge states are constrained to be

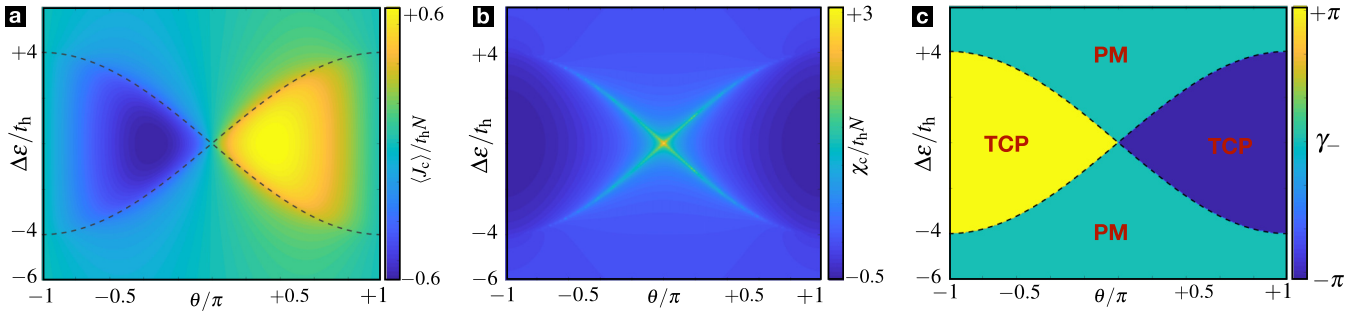


FIG. 6. Phase diagram of the noninteracting Creutz ladder. (a) The persistent circulating chiral current $\langle J_c \rangle$ in Eq. (25) is represented by a contour plot and clearly displays a large nonzero value inside two lobes that touch at $\theta = 0$, surrounded by a region with a vanishingly small particle flow. (b) Contour plot for the chiral susceptibility χ_c in Eq. (26), the maxima of which show a divergence with the number of sites N_s that delimits the lobes with a large nonzero chiral current, and marks the onset of a quantum phase transition. (c) Contour plot of Zak's phase in Eq. (28) as a function of the flux and imbalance. We see that the two lobes with a large chiral flow correspond to the regions where the system is a topological crystalline phase with $\gamma_{\pm} = \pm\pi$, here represented by yellow/blue colors. The phase diagram thus consists of two regions with a topological-crystalline state that supports a large persistent chiral current except for $|\theta| \rightarrow \pi$, surrounded by a trivial band insulator with a vanishingly small chiral current. The dashed black line of (a) shows the transition points from the topological to the trivial phases marked by the change of Zak's phase Eq. (29), which agrees perfectly with the points where the chiral susceptibility diverges.

zero-energy modes. In the present case, the underlying sublattice symmetry is broken, as $\{h(k), \sigma^y\} \neq 0$ for $\theta \neq \pi$. As a consequence, the topological phase is no longer within the AIII class, such that the edge states are no longer restricted to have zero energies. Even if no global symmetry is responsible for the protection of this topological phase, one can find a pointlike inversion symmetry,

$$c_{i,u} \mapsto c_{N_s-i,d}, \quad c_{i,d} \mapsto c_{N_s-i,u}, \quad (30)$$

under which the Hamiltonian remains invariant $H_{\text{CH}} \mapsto H_{\text{CH}}$. Accordingly, ground states with a quantized Zak phase can be understood as instances of a TCP [158–160]. Note that the above circulating chiral current Eq. (19) is also preserved under this ladder inversion $J_c \mapsto J_c$. The ground state can thus simultaneously display a nonzero topological invariant protected by inversion symmetry and a nonzero persistent circulating current, departing in this way from other topological crystalline insulators. Note that, in contrast to the two-dimensional quantum Hall effect, this circulating current is not carried by the edge states, which remain localized at the left/right boundaries. In Fig. 6(c), we represent the contour plot of Zak's phase Eq. (28) as a function of $(\theta, \Delta\varepsilon/t_h)$. By comparing to the contour plot of the chiral current in Fig. 6(a), we see that the two lobes with a large circulating chiral flow correspond to regimes with nonzero $\gamma_{\pm} = \pm\pi$, in which the ground state is a topological phase. As $\theta \rightarrow 0$, the topological insulator regions give way to a trivial band insulator with a vanishingly small current. On the other hand, as $\theta \rightarrow \pm\pi$ toward the other time-reversal configurations, the circulating chiral current vanishes while the ground state still supports a nonzero Zak's phase that ultimately yields the π -flux results of Ref. [131]. In the following sections, we explore how this picture gets modified as we include Hubbard interactions, starting from strong interactions.

B. Dzyaloshinskii-Moriya superexchange

In this section, we discuss the nature of the phase diagram in the strong-coupling limit $V_v \gg t_h$ [i.e., $g^2 \gg 1$ in

the language of the GN model Eqs. (4)]. As mentioned in the Introduction, in the strong-coupling regime, the half-filled rectangular Hubbard ladder for spin-full fermions can be described in terms of an effective antiferromagnetic Heisenberg ladder, where the origin of the spin-spin interactions can be understood as a superexchange mechanism [48]. As shown in Ref. [131], the strong-coupling limit changes considerably for the cross-linked geometry in the π -flux limit. Here, one obtains ferromagnetic Ising interactions with a \mathbb{Z}_2 symmetry instead of the SU(2)-invariant Heisenberg couplings. In the Ising case, one finds a symmetry-broken ferromagnet with magnetization $M_y \neq 0$ or, equivalently [142], a pseudoscalar condensate $\Pi_0 \neq 0$ in the language of the GN model. In both cases, there is a spontaneous symmetry breaking (SSB) process where the corresponding AIII topological insulator gives way to this long-range-ordered phase that breaks the \mathbb{Z}_2 symmetry. Since we have shown above that a current-carrying topological phase also appears for generic fluxes $\theta \neq 0$, it is interesting to explore if there is a similar SSB where it disappears in favor of a long-range order.

In the strong-coupling regime, due to the nature of the synthetic Hubbard interactions, the low-energy subspace will be spanned by fermion configurations that avoid double occupancies of two vertically-neighboring sites of the ladder, as these doublons pay a large energy penalty. The leading-order dynamics comes from second-order processes $\mathcal{O}(t_h^2/V_v)$ where fermions tunnel back and forth virtually populating these doublons. At half filling, all the possible second-order processes can be written in terms of orbital spin operators:

$$\begin{aligned} T_i^x &= \frac{1}{2}(c_{i,u}^\dagger c_{i,d} + c_{i,d}^\dagger c_{i,u}), \\ T_i^y &= \frac{i}{2}(c_{i,d}^\dagger c_{i,u} - c_{i,u}^\dagger c_{i,d}), \\ T_i^z &= \frac{1}{2}(c_{i,u}^\dagger c_{i,u} - c_{i,d}^\dagger c_{i,d}). \end{aligned} \quad (31)$$

The second-order superexchange processes lead to the following effective Hamiltonian of coupled orbital spins:

$$H_{\text{DM}} = \sum_i (J(1 + \xi)T_i^x T_{i+1}^x + J(1 - \xi)T_i^y T_{i+1}^y) + \sum_i (\mathbf{D} \cdot (\mathbf{T}_i \times \mathbf{T}_{i+1}) + hT_i^z), \quad (32)$$

where we have introduced the couplings

$$J = \frac{4t_h^2}{V_v} \cos \theta, \quad \xi = \sec \theta, \quad \mathbf{D} = -\frac{4t_h^2}{V_v} \sin \theta \mathbf{e}_z, \quad h = \Delta\epsilon. \quad (33)$$

The first line of Eq. (32) represents the so-called XY model [161,162] with spin-spin coupling strength J and anisotropy parameter ξ given in Eqs. (33). The second line of Eq. (32) contains a so-called *Dzyaloshinskii-Moriya interaction* [163,164], which contains an antisymmetric superexchange with the coupling \mathbf{D} given in Eqs. (33). Additionally, there is an external transverse field h also defined in Eqs. (33).

Let us note that in the π -flux regime $\theta = \pi$, the Dzyaloshinskii-Moriya coupling and the xx interactions vanish $\mathbf{D} = \mathbf{0}$, $J(1 + \xi) = 0$, while the yy interactions $J(1 - \xi) = -8t_h^2/V_v$ lead to the aforementioned Ising coupling, which favors a ferromagnetic long-range order along the y axis, which coincides with the results of Refs. [131]. Conversely, for vanishing flux $\theta = 0$, it is $\mathbf{D} = \mathbf{0}$, $J(1 - \xi) = 0$ which vanish, while the xx interactions $J(1 + \xi) = +8t_h^2/V_v$ favor an antiferromagnetic long-range order. We thus expect that, as one varies the external magnetic flux, the direction and character of the long-range order within the xy plane will be modified.

Fortunately, the effective model turns out to be exactly solvable via Jordan-Wigner [165] and Bogoliubov [166] transformations. The first one allows us to express the orbital spin model in terms of a chain of spinless fermions, which in momentum space yields

$$H_{\text{DM}} = \sum_{k \in \text{HBZ}} \chi_k^\dagger (\tilde{\epsilon}_0(k) \mathbb{I}_2 + \tilde{\mathbf{d}}(k) \cdot \boldsymbol{\sigma}) \chi_k. \quad (34)$$

Here, we have introduced the Nambu spinor $\chi_k = (f_k^\dagger, f_{-k})^t$, which is expressed in terms of the new creation-annihilation operators of the Jordan-Wigner fermions within the halved Brillouin zone $\text{HBZ} = [0, \pi/a]$. The quadratic Hamiltonian in Eq. (34) depends on the scalar and vector functions

$$\tilde{\epsilon}_0(k) = \frac{4t_h^2}{V_v} \sin \theta \sin(ka),$$

$$\tilde{\mathbf{d}}(k) = \frac{4t_h^2}{V_v} \sin(ka) \mathbf{e}_y + \left(\Delta\epsilon - \frac{4t_h^2}{V_v} \cos \theta \cos(ka) \right) \mathbf{e}_z, \quad (35)$$

which play an analogous role to those defined in Eqs. (6) for the noninteracting limit of the Creutz-Hubbard ladder. Note, however, that the number of spinless Jordan-Wigner fermions is not conserved, as the transformed spin model is not invariant under $U(1)$ symmetry. Applying now a Bogoliubov transformation yields two energy bands analogous to

Eq. (7):

$$\tilde{\epsilon}_\pm(k) = \tilde{\epsilon}_0(k) \pm |\tilde{\mathbf{d}}(k)|. \quad (36)$$

The ground-state energy, in this case, will be determined by filling all the momenta for which $\tilde{\epsilon}_\pm(k) < 0$, which need not be N_s fermions as occurs for the original half-filled ladder with $U(1)$ symmetry. Therefore, the presence of a gap-closing phase transition can be predicted by finding the set of microscopic parameters that allow for $\tilde{\epsilon}_\pm(k_0) = 0$ for some $k_0 \in \text{HBZ}$. One can only find a solution of this equation for a specific momentum $k_0 \in \{0, \pi/a\}$ if for $\Delta\epsilon = \mp(4t_h^2/V_v) \cos \theta$. Accordingly, we identify two lines of second-order phase transitions at

$$\Delta\epsilon_c(\theta) = \pm \frac{4t_h^2}{V_v} |\cos \theta|. \quad (37)$$

Let us now discuss the different phases that are delimited by these critical lines. In addition to the aforementioned SSB ferromagnetic and antiferromagnetic phases, the limit $h \gg |J|, |\mathbf{D}|$ can be easily understood. In this case, the orbital spins align in the opposite direction of the transverse field Eq. (32), which can be understood as an orbital PM in which the original fermions are localized to the sites of the lower leg of the ladder. In Fig. 7, we present some observables that allow us to understand how these three different phases are arranged in this strong-coupling limit: (i) an antiferromagnet (AFM_x) aligned along the x axis occurs for $\Delta\epsilon < \Delta\epsilon_c(\theta)$ and $\theta \in (-\pi/2, \pi/2)$, (ii) a ferromagnet (FM_y) aligned along the y axis occurs for $\Delta\epsilon < \Delta\epsilon_c(\theta)$ and $\theta \in [-\pi, -\pi/2) \cup (\pi/2, \pi]$, and (iii) a PM with all spins anti-aligned with the transverse field appears for $\Delta\epsilon > \Delta\epsilon_c(\theta)$ for any flux $\theta \in [-\pi, \pi]$ for sufficiently large transverse fields. In Fig. 7(a), we represent the two-point correlations functions $\langle T_1^x T_{N_s}^x \rangle$ in the ground state of the orbital spin model, which tend to the AFM order parameter in the thermodynamic limit $|\langle T_1^x T_{N_s}^x \rangle| \rightarrow \langle T_1^x \rangle^2 = M_x^2$, which clearly displays a nonzero value in the inner yellow lobe. In Fig. 7(b), we represent the two-point correlations functions $\langle T_1^y T_{N_s}^y \rangle$ in the ground state of the orbital spin model, which tend to the FM order parameter in the thermodynamic limit $|\langle T_1^y T_{N_s}^y \rangle| \rightarrow \langle T_1^y \rangle^2 = M_y^2$, which clearly displays a nonzero value in two yellow lobes that touch the AFM_x phase at $\theta = \pm\pi/2$. Finally, in Fig. 7(c), we represent the transverse magnetization $|\langle T_i^z \rangle|$, which becomes larger in the PM regions around the orbital magnets.

As noted at the end of the previous section, the TCPs supporting a persistent chiral current at zero interactions should disappear in favor of orbital magnetic phases as one increases the Hubbard interactions. The current strong-coupling analysis shows that these orbital magnets correspond to an AFM_x or FM_y depending on the magnetic flux. Additionally, the trivial band insulators that appear in the noninteracting limit should be adiabatically connected to the PM phases, as they both describe a limiting case in which all fermions occupy the sites of the lower leg for a very large energy imbalance. The questions that will be addressed in the following section are how these two limiting cases are connected, what the nature is of the quantum phase transitions that appear along the way, and how the chiral current/susceptibility can be used to characterize them.

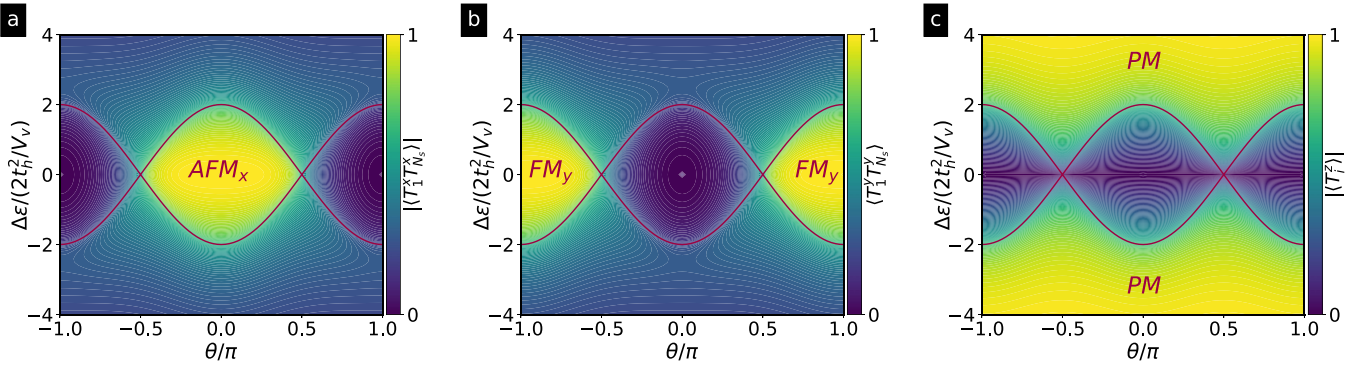


FIG. 7. Phase diagram of the Creutz ladder for strong interactions. Phase diagram displaying three different phases: ferromagnetic FM_y , antiferromagnetic AFM_x , and paramagnetic PM phases. The horizontal axis represents the flux per plaquette, whereas the vertical axis corresponds to the ratio of the energy imbalance to the superexchange strength J . (a) The correlator $\langle T_1^y T_N^x \rangle$ is represented by a contour plot, quantitatively distinguishing a central yellow lobe where this correlator displays AFM_x long-range order. (b) We also represent the correlator $\langle T_1^x T_N^y \rangle$, which instead captures two lateral yellow lobes displaying FM_y long-range order. (c) The contour plot of the magnetization along the z direction $|(T^z)|$ captures the paramagnetic phases, here represented by the yellow surrounding regions. The red lines correspond to the critical line in Eq. (37), and perfectly delimit the regions where the above observables characterize the various phases.

V. PHASE DIAGRAM: SELF-CONSISTENT HARTREE-FOCK METHOD AND VARIATIONAL MATRIX-PRODUCT STATES

To address the question raised at the end of the previous section and explore the full phase diagram of the model in the $\{\Delta\epsilon, \theta, V_v\}$ volume, we use two different methods: (i) a self-consistent mean-field approximation [167] and (ii) a variational method based on MPSs [58].

With regard to the first one, we start from the Hubbard interactions Eq. (2) and perform the Hartree-Fock decoupling

$$\begin{aligned} \frac{1}{2} \sum_{\ell} c_{i,\bar{\ell}}^{\dagger} c_{i,\ell}^{\dagger} c_{i,\ell} c_{i,\bar{\ell}} &\approx \langle c_{i,u}^{\dagger} c_{i,u} \rangle c_{i,d}^{\dagger} c_{i,d} + \langle c_{i,d}^{\dagger} c_{i,d} \rangle c_{i,u}^{\dagger} c_{i,u} \\ &- \langle c_{i,u}^{\dagger} c_{i,d} \rangle c_{i,d}^{\dagger} c_{i,u} - \langle c_{i,d}^{\dagger} c_{i,u} \rangle c_{i,u}^{\dagger} c_{i,d}, \end{aligned} \quad (38)$$

where we have neglected a c number that will contribute equally to the energies of all possible eigenstates of the mean-field Hamiltonian. After this Hartree-Fock decoupling, the Hamiltonian Eqs. (1) and (2) is expressed as the sum of quadratic terms

$$\begin{aligned} H_{CH}^{\text{mf}} = \sum_{i,\ell} &\left(t_h e^{-i\frac{s_{\ell}\theta}{2}} c_{i+1,\ell}^{\dagger} c_{i,\ell} + t_d c_{i+1,\ell}^{\dagger} c_{i,\bar{\ell}} - \frac{s_{\ell} \Delta\epsilon}{2} c_{i,\ell}^{\dagger} c_{i,\ell} \right. \\ &\left. + \frac{1}{2} \epsilon_{\ell}(\{n_{i,\bar{\ell}}\}) c_{i,\bar{\ell}}^{\dagger} c_{i,\ell} + t_{\ell}(\{b_{i,\bar{\ell}}\}) c_{i,\ell}^{\dagger} c_{i,\bar{\ell}} + \text{H.c.} \right). \end{aligned} \quad (39)$$

Here we have introduced a shift of the on-site energies ϵ_{ℓ} that depends on the local fermion numbers $n_{i,\bar{\ell}} = \langle c_{i,\bar{\ell}}^{\dagger} c_{i,\bar{\ell}} \rangle$, together with a vertical tunneling term t_{ℓ} that depends on the bond densities $b_{i,\bar{\ell}} = \langle c_{i,\bar{\ell}}^{\dagger} c_{i,\ell} \rangle$. The former, which is always a real number, will play an important role when the fermions distribute differently along the two legs of the ladder; whereas the latter, which can be a complex number, shall determine how the fermions delocalize over the vertical links of the ladder. These parameters are both proportional to the Hubbard

interaction:

$$\epsilon_{\ell}(\{n_{i,\bar{\ell}}\}) = V_v \langle c_{i,\bar{\ell}}^{\dagger} c_{i,\bar{\ell}} \rangle, \quad t_{\ell}(\{b_{i,\bar{\ell}}\}) = V_v \langle c_{i,\bar{\ell}}^{\dagger} c_{i,\ell} \rangle. \quad (40)$$

The on-site energy shifts will renormalize the energy imbalance, changing in accordance with the extent of the noninteracting phases. In addition, the vertical tunnelings can change the physics considerably, as they modify the effective connectivity of the ladder. In the noninteracting case, interleg tunnelings can only occur via cross-link hoppings whereas, in the presence of interactions, these mean-field terms can allow for such hoppings occurring vertically.

We note that the mean-field approximation requires the observables $\{n_{i,\ell}, b_{i,\ell}\}_{i=1}^N$ to be determined self-consistently, and we must deal with a number of self-consistency equations that grows linearly with the number of sites. The self-consistent loop consists in the following steps: (i) We start by setting an initial configuration of densities $\{n_{i,\ell}\}$ and bond densities $\{b_{i,\ell}\}$ for different phases. With regard to the AFM_x ordering, we have chosen a pattern of real numbers with alternating signs for bond densities $\{b_{i,\ell}\}$ and alternation of 0 and 1 for $\{n_{i,\ell}\}$ such that $\sum_i (n_{i,u} + n_{i,d}) = N_s$. Instead, when the target is the TCP or the FM_y , it is better to start from a translationally invariant pattern of complex numbers for $\{b_{i,\ell}\}$. Moreover, for the PM phase, we start from a translationally invariant pattern of real numbers for $\{b_{i,\ell}\}$ and we fixed $n_{i,u} = 1$ and $n_{i,d} = 0 \forall i$. (ii) Given these initial seeds, we diagonalize the fermionic tight-binding model defined in Eq. (39) and get another estimate of the mean-field parameters Eqs. (40). We then iterate this process until the self-consistent parameters and the energy converge with an error of 10^{-8} for lattices up to $N_s = 64$.

Let us now discuss these different mean-field configurations at the level of the continuum QFT Eqs. (9). Assuming a translationally invariant half-filled ground state, one finds that an occupation imbalance on the legs $\Delta n_i = n_{i,u} - n_{i,d} = \Delta n$, $\forall i$ shifts the Wilson masses in Eqs. (12) as follows:

$$m_{\pm} c^2 \mapsto \tilde{m}_{\pm} c^2 = \frac{\Delta\epsilon - V_v \Delta n}{2} \mp 2t_h \sin\left(\frac{\theta}{2}\right). \quad (41)$$

This can readily be interpreted as the aforementioned renormalization of the energy imbalance $\Delta\epsilon \rightarrow \Delta\tilde{\epsilon}$. A positive bare energy imbalance $\Delta\epsilon > 0$ favors the occupation of fermions on the lower leg $\Delta n < 0$, which in turn increases the renormalized energy imbalance $\Delta\tilde{\epsilon} = \Delta\epsilon + V_v|\Delta n|$ in Eq. (41). Consequently, the critical lines where one of the Wilson masses Eq. (29) gets inverted will be shifted toward smaller values of the bare energy imbalance $\Delta\epsilon$ when the Hubbard interactions are increased, such that the self-consistent topological regions shrink in favor of the mean-field trivial band insulator.

Motivated by the strong-coupling results of the previous section, another possibility for a translationally invariant ground state is that of a purely imaginary bond density $b_{i,u} = \langle c_{i,u}^\dagger c_{i,d} \rangle = -b_{i,d} = iM_y$, $\forall i$. Such arrangement of bond densities corresponds to the orbital ferromagnet FM_y found in the previous section for sufficiently strong couplings and fluxes. This type of order is induced by the mean-field vertical tunnelings Eqs. (40) and, in the continuum QFT Eqs. (9), leads to a unique mass term:

$$m_\eta c^2 \bar{\Psi}_\eta \Psi_\eta \rightarrow \tilde{m}_\eta c^2 \bar{\Psi}_\eta \Psi_\eta + \eta V_v M_y \bar{\Psi}_\eta \gamma_\eta^5 \Psi_\eta. \quad (42)$$

These two self-consistent masses are renormalized by the imbalance and bond densities, which correspond to the aforementioned scalar and pseudoscalar condensates of the GN model with a Wilsonian regularization [142]. If the interactions are strong enough, the ferromagnet will be formed $M_y \neq 0$, such that the Zak's phase will no longer be quantized Eq. (29) as a consequence of the two nonzero masses. Moreover, the long-range order is incompatible with the protecting symmetries, and the ferromagnet fully expels the TCP via a SSB phase transition.

Again motivated by the strong-coupling results, we should consider a bond-density wave that breaks translation invariance. This is given by a purely real alternating bond density $b_{i,u} = \langle c_{i,u}^\dagger c_{i,d} \rangle = b_{i,d} = (-1)^i M_x$, $\forall i$, corresponding to the orbital anti-ferromagnet AFM_x , which was found for sufficiently strong couplings and small magnetic fluxes (see Fig. 7). In light of this order parameter, we see that in the limit $M_x \rightarrow 1$, fermions delocalize along the vertical rungs of the ladder with an alternating symmetric/antisymmetric pattern. Such an alternating pattern leads to a different long-wavelength term, as it effectively couples the two species of Dirac fermions by the following Umklapp term:

$$m_\eta c^2 \bar{\Psi}_\eta \Psi_\eta \rightarrow \tilde{m}_\eta c^2 \bar{\Psi}_\eta \Psi_\eta - V_v M_x \bar{\Psi}_\eta \Psi_\eta. \quad (43)$$

At zero magnetic flux, where the band structure in Fig. 5 displays a flat band and a cosine band, one may form a massless Dirac spinor from the right- and left-moving components at $k_\pm = \pm\pi/2a$, such that the gap-opening Umklapp term corresponds to yet a different mass term. Although at the mean-field level [13], the massless Dirac fermion is unstable toward the alternating bond-density wave for arbitrary-small interactions, the presence of the flat band and the correlations beyond mean-field may change this simple picture. In any case, if this bond-density wave is formed, the topological invariant will no longer be quantized Eq. (29) and the associated antiferromagnet will fully expel the topological phase.

Let us note that this self-consistent mean-field method is equivalent to a large- N limit of the equivalent GN model, where one introduces auxiliary bosonic fields via a Hubbard-Stratonovich transformation [168] and sends the number of fermionic species $N \rightarrow \infty$. In the π -flux limit, it suffices to introduce a couple of auxiliary fields, the nonzero expectation values of which lead to the onset of the so-called scalar and pseudoscalar condensates discussed in Sec. II B. We have checked that our self-consistent mean-field approach provides numerical results that are in complete agreement with the large- N prediction of the π -flux limit presented in Ref. [142]. As one modifies the magnetic flux, the large- N approach should be generalized to include an additional auxiliary field, the condensation of which would be connected to the AFM_x order. Instead of following this approach, which requires solving a new set of coupled nonlinear gap equations, the current self-consistent mean-field is sufficiently general so it can directly encompass any type of ordering, and such an order can be efficiently found by a suitable choice of the initial seed.

In any case, both the mean-field and the large- N methods do not take the interparticle correlations in full account. For this reason, we benchmark these results with MPS methods. In particular, we use the DMRG based on MPSs, which is becoming a very useful tool to explore lattice discretizations of quantum field theories [36,169]. This can be considered as the most stringent test of the validity of the mean-field approach. We consider lattices up to $N_s = 128$ sites and virtual dimension up to $\chi = 200$. Our DMRG code is based on MPSs and uses a two-site optimization scheme. It is built implementing the Abelian symmetries such as a particle conservation. Indeed, we fix half-filling and open boundary conditions.

A. Weak and intermediate interactions

In this section, we analyze the effect of correlations in the phase diagram of the Creutz-Hubbard ladder under a generic magnetic flux, focusing on the regime of weak interactions.

We start by setting $V_v/t_h = 1.0$ and $V_v/t_h = 2.0$, which correspond to the red and green shaded planes of the schematic phase diagram of Fig. 2. Our numerical results for the phases of matter that appear in these planes are presented in Fig. 8, where we have used self-consistent mean-field and DMRG methods. The lines represent the critical points where the topological and SSB phase transitions occur, either obtained with a DMRG method based on finite MPS with bond dimension $\chi = 200$ (red stars) or by the self-consistent Hartree-Fock method (yellow dashed lines). As can be observed in the figure, for weak interactions, the Hartree-Fock and DMRG critical points separating the TCP and PM regions yield two critical lines that are very similar to each other. The main differences appear in the critical lines separating the AFM_x and PM phases, as the mean-field method predicts a smaller AFM_x . Let us now analyze this figure in more detail and describe the methodology used to extract these critical points.

In analogy with the noninteracting case Eq. (1), the ground state of the weakly interacting Creutz-Hubbard ladder Eq. (2) contains a TCP as one departs from the π -flux limit. As discussed qualitatively around Eq. (41), one of the expected

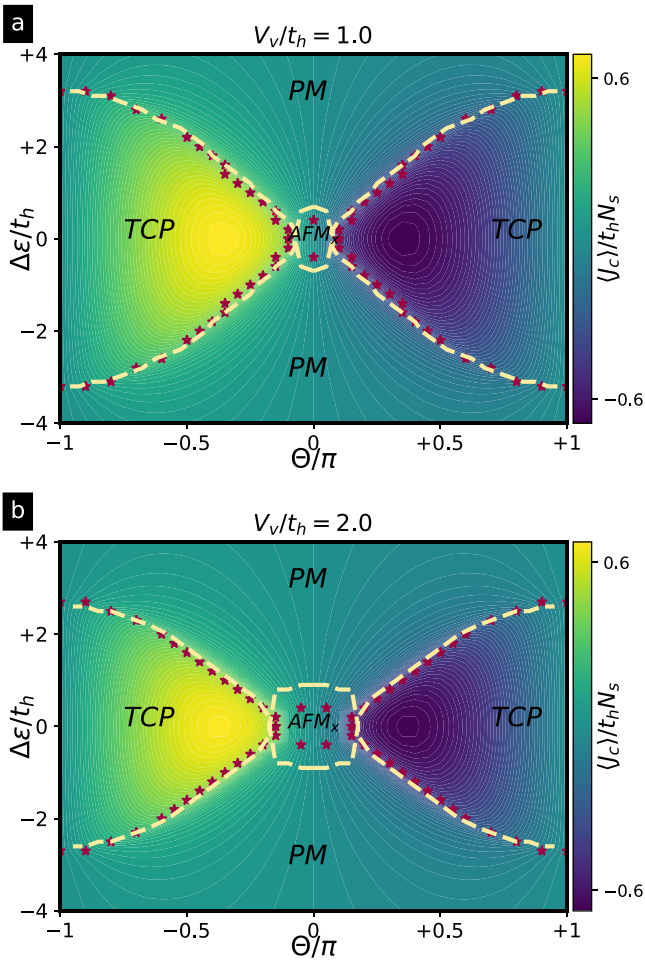


FIG. 8. Phase diagrams for weak interactions. (a) $V_v/t_h = 1$, (b) $V_v/t_h = 2$: The phase diagrams display two regions hosting a topological crystalline phase (TCP), a long-range-ordered antiferromagnetic phase (AFM_x), and a paramagnetic phase (PM). The horizontal axis represents the magnetic flux, whereas the vertical axis corresponds to the ratio of the energy imbalance to the tunneling strength. The red stars (yellow dashed lines) show the critical points found from DMRG (self-consistently mean-field) numerics. These points are plotted on top of the contour plot of the chiral current, obtained by calculating Eq. (19) using DMRG.

effects of interactions is to shrink the size of the TCP lobes in favor of the trivial band insulator. Note that the trivial band insulator is adiabatically connected to the orbital PM when the energy imbalance is increased, and we refer to them interchangeably. This shrinking can be readily observed by comparing the vertical extent of the TCP lobes in the noninteracting and interacting cases (compare Figs. 6 and 8). Moreover, as shown in Sec. VC, the entanglement spectrum on these lobes is twofold degenerate—see Fig. 15 a hallmark of symmetry-protected topological phases [170]. This shows that the noninteracting TCPs discussed in Sec. IV A are adiabatically connected to these correlated TCP lobes. Comparing Figs. 8(a) and 8(b), we also see that the shrinking of the TCP in favor of the PM increases with the strength of the Hubbard interactions, which is a direct consequence of the interaction-induced renormalization of the Dirac-fermion masses Eq. (41) in the continuum QFT.

Let us also recall that, as argued in Sec. III, the violation of Lorenz symmetry in the continuum QFT Eqs. (15) and (16) can be associated to a different propagation speed for right- and left- moving particles (see the insets of Fig. 3). This difference can give rise to a net circulating chiral current, serve to characterize further the phases of the model, and may act as a good indicator to predict the critical lines [see Figs. 6(a) and 6(b)] In particular, we recall that the noninteracting TCP supports large values of this permanent chiral current away from the π -flux limit [see Fig. 6(a)]. In the background of Figs. 8(a) and 8(b), we present the expectation value of the chiral current $\langle J_c \rangle$ in Eq. (19) in the presence of interactions, as obtained by the DMRG numerics. We see that, as the TCP lobes shrink in size due to the Hubbard interactions, the area with a large chiral current also decreases. Therefore, the correlated TCPs can still support large chiral currents around the ladder.

The critical points delimiting the TCP lobes in the phase diagram are estimated via the chiral susceptibility $\chi_c = \partial \langle J_c \rangle / \partial \theta$ Eq. (26). We recall that, in the noninteracting limit, this susceptibility presents a divergence at the critical points [see Fig. 6(b)]. In Fig. 9(a), we display the chiral susceptibility for ladders with a different number of sites per leg $N_s \in \{16, 32, 64\}$, fixing the energy imbalance $\Delta\epsilon = 0.4t_h$ and interaction strength $V_v = 2t_h$, and varying the external magnetic flux. These numerical results clearly show a peak at two symmetric values of the magnetic flux with respect to the zero-flux axis. The finite size scaling (FSS) of the chiral susceptibility maxima as a function of N is displayed in the inset. As one can see in the inset, the peak of the chiral susceptibility diverges with the size of the ladder, and fitting the maxima of θ_c to $\theta_c(N) = \theta_c(1 + aN^{-1} + bN^{-2})$, we can delimit the TCP lobes and locate the phase transitions. In Fig. 9(b), we show the contour plot of the chiral susceptibility with the corresponding peaks, which clearly shows how the critical lines separate the TCP from other phases. Comparing to the noninteracting case in Fig. 6(b), we clearly see that these critical points are moved towards smaller imbalances, which underlies the shrinking of the TCP lobes.

So far, our numerical benchmark has focused on the TCP phase, and revolved around quantities related to the circulating chiral current. An alternative way of identifying this phase boundary is by studying the occupation leg imbalance:

$$\Delta n = \frac{1}{N_s} \sum_j (\langle c_{j,u}^\dagger c_{j,u} \rangle - \langle c_{j,d}^\dagger c_{j,d} \rangle). \quad (44)$$

The occupation imbalance is induced by a nonzero energy imbalance $\Delta\epsilon$, which motivates the definition of an imbalance susceptibility $\chi_{\Delta n} = \partial \Delta n / \partial \Delta\epsilon$ that proved to be a good indicator of the quantum phase transition in the π -flux limit [131], and can be easily calculated using our DMRG code. In Fig. 9(c), we show the imbalance susceptibility for ladders with a different number of sites per leg $N_s \in \{16, 32, 64\}$, fixing the magnetic flux to $\theta = 3\pi/4$, the Hubbard interactions to $V_v = 2t_h$, and varying the energy imbalance $\Delta\epsilon$. Once again, this susceptibility shows a pair of peaks that are symmetric with respect to the zero-imbalance axis. A FSS shows that this peak actually diverges in the thermodynamic limit and allows us to locate the position of the critical point. The

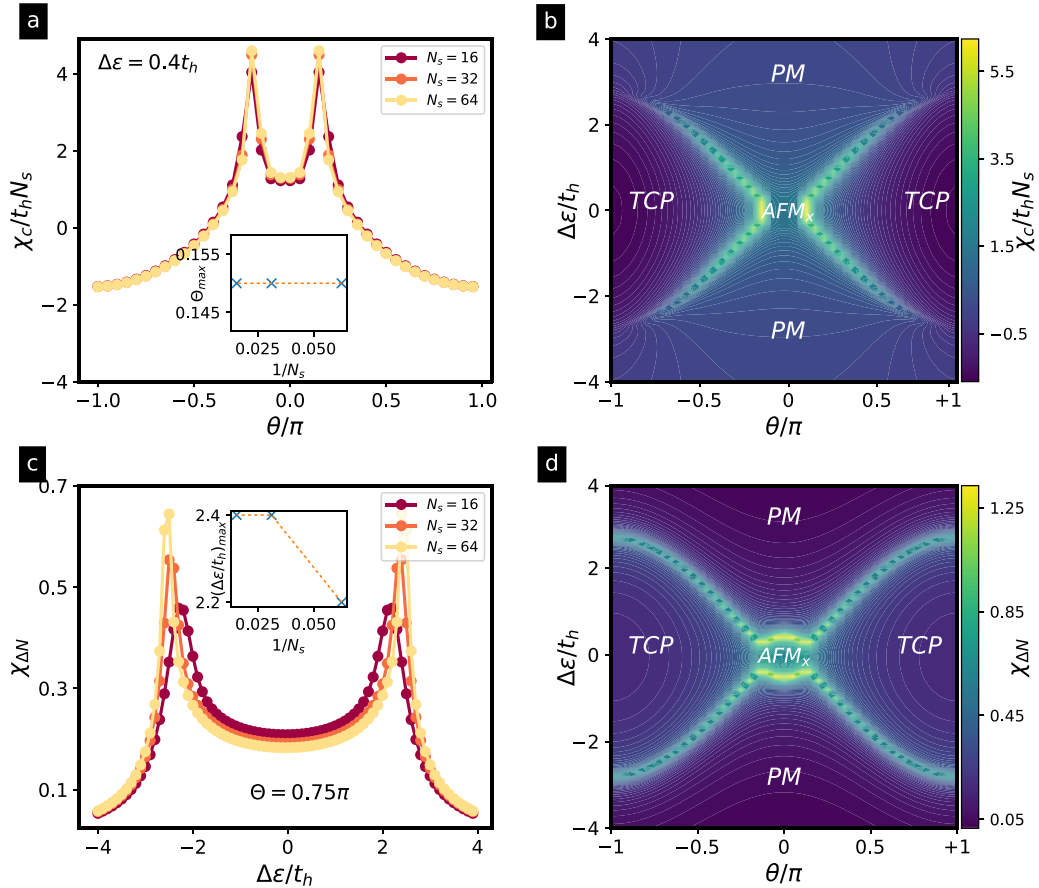


FIG. 9. Chiral and imbalance susceptibilities. (a) The peaks of the chiral susceptibility χ_c with growing system size $N_s \in \{16, 32, 64\}$ allow us to locate the critical point for a cut of phase diagram at $V_v = 2t_h$ and $\Delta\epsilon = 0.4t_h$. (b) The contour plot of the chiral susceptibility for system size $N_s = 64$, delimiting the TCP lobes from other phases. (c) The peaks of the imbalance susceptibility $\chi_{\Delta n}$ with growing system size $N_s \in \{16, 32, 64\}$ allow us to locate the critical points also around the π -flux regime. (d) The contour plot of the imbalance susceptibility for system size $N_s = 64$.

critical points obtained through this analysis are represented in a contour plot in Fig. 9(d). As can be seen from these results, this susceptibility is more effective than the chiral one in the critical regions around π flux, which is to be expected since the chiral current vanishes in these regions.

The main difference brought up by the interactions occurs in the region of small magnetic fluxes, where the Umklapp term Eq. (43) may dominate over the other gap-opening mechanisms. This term is expected to stabilize a bond-ordered-wave with fermions delocalized along the vertical bonds of the ladder in alternating symmetric/antisymmetric orbitals, resembling an orbital AFM_x . Our numerics show that there are additional critical lines that separate this small-flux region from either the TCP lobes at higher flux or the orbital PM at higher energy imbalances (see Fig. 8). As supported by the numerical results presented in the following paragraphs, this intermediate region hosts AFM_x long-range order due to SSB of a global \mathbb{Z}_2 invariance. To accurately extract the critical points between the AFM_x and PM, we calculate the staggered magnetization

$$M_x = \frac{1}{N_s} \sum_j (-1)^j (\langle c_{j,u}^\dagger c_{j,d} \rangle + \langle c_{j,d}^\dagger c_{j,u} \rangle), \quad (45)$$

which corresponds to the order parameter of the alternating bond density wave. The advantage of the strong-coupling perspective Eq. (32) is that one identifies the energy imbalance as the transverse magnetic field Eq. (33), and one can readily define the antiferromagnetic susceptibility as $\chi_{M_x} = \partial M_x / \partial \Delta\epsilon$. In Fig. 10(a), we present the staggered magnetization M_x for different system sizes. The crossing of the lines in the main panel serves to obtain the critical point of the model for weak fluxes. As proved by the data collapse shown in the inset of Fig. 10(a), the critical exponents correspond to those of the $(1+1)$ Ising universality class.

Moreover, we also want to address if the strong-coupling AFM_x phase, which appears for vanishingly small fluxes, also sets for arbitrarily small values of the interaction strength V_v , or if a PM sets in before the AFM_x order takes on. For this aim, we will study the phase diagram sketched in Fig. 2 fixing the flux θ , and varying the imbalance $\Delta\epsilon$ and the interactions V_v , that permit us to explore different planes also the correlation effects at intermediate interactions. We set $\theta = 0.25\pi$ and $\theta = 0$, which correspond to the green and brown shaded planes of the schematic phase diagram of Fig. 2. Our numerical results for the phases of matter that appear in these planes are presented in Fig. 11, where we have used the self-consistent mean-field (yellow dashed line) and DMRG

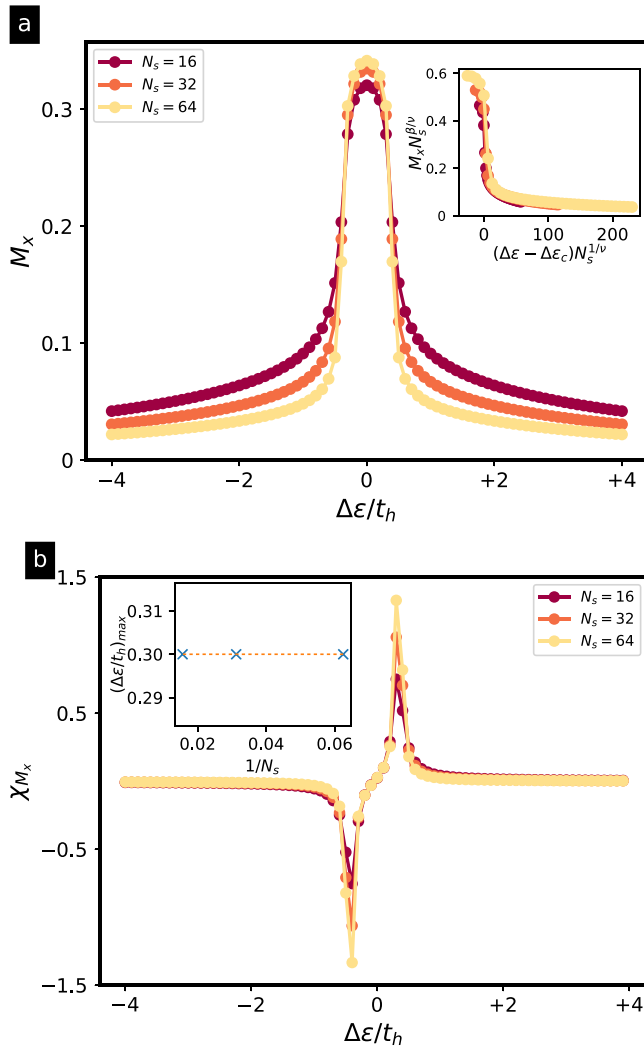


FIG. 10. Staggered magnetization and magnetic susceptibility. (a) Staggered magnetization for fixed interaction strength $V_v = 2t_h$ and flux $\theta = \pi/10$, and different number of sites per length $N_s \in \{16, 32, 64\}$. As the length increases, the systems develop a nonzero expectation value only within a symmetric region around zero imbalance. (b) The magnetic susceptibility χ_{M_x} for the same parameters shows a couple of peaks that increase with the system size and allow us to locate the critical points.

methods (red stars) to determine the critical lines. In the background, we present a contour plot that serves as a guide to the eye to identify the different phases. As shown in the figure, the red stars obtained with a DMRG method based on finite MPS with bond dimension $\chi = 200$ yield a much better estimate of the critical lines that separate the different phases.

Let us start discussing the case of $\theta = 0.25\pi$ shown in Fig. 11(b). Here, one can distinguish three different phases: TCP, PM, and AFM_x . As can be observed in the figure for weak interaction, the Hartree-Fock and DMRG critical points separating the TCP and PM regions yield two critical lines similar to each other, although differences arise as the interactions are increased. Moreover, the weak-coupling limit can be understood as a ferromagnetic coupling between the two chains in the spin model description (as shown in Appendix). Along this line the central charge c is equal to 1.

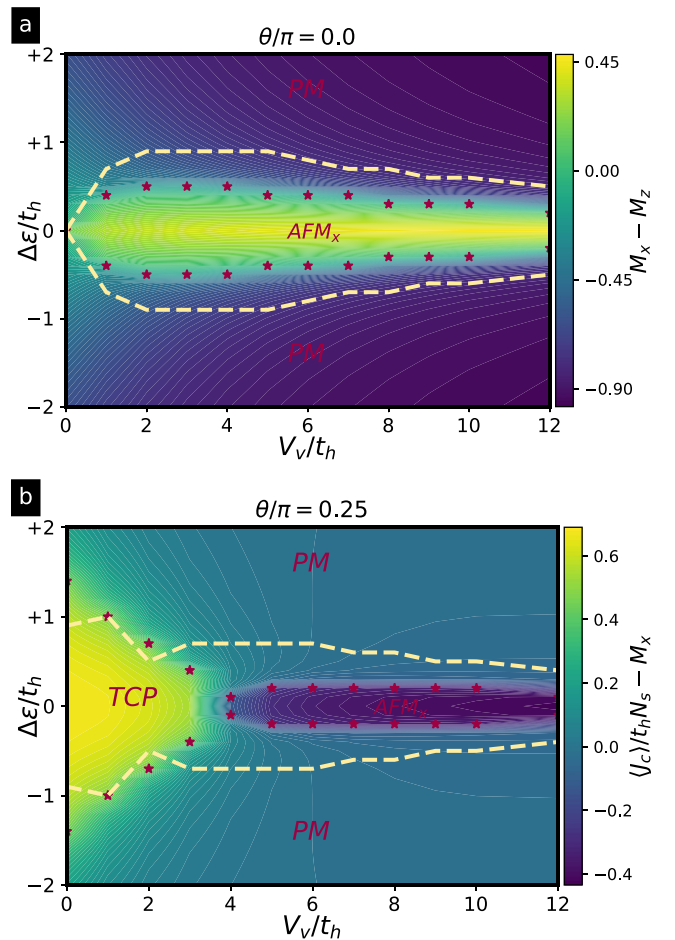


FIG. 11. Phase diagram in the plane $(V_v, \Delta\epsilon)$ for fixed flux. (a) The phase diagram for $\theta = 0.0$ displays two regions hosting a long-range-ordered antiferromagnetic phase (AFM_x), and a paramagnetic phase (PM). (b) The phase diagram for $\theta = 0.25\pi$ displays a region hosting a topological crystalline phase (TCP), a long-range-ordered antiferromagnetic phase (AFM_x), and a paramagnetic phase (PM). The horizontal axis represents the ratio of interaction to the tunneling strength, whereas the vertical axis corresponds to the ratio of the energy imbalance to the tunneling strength. The red stars (yellow dashed lines) show the critical points found from DMRG (self-consistently mean-field) numerics. These points are plotted on top of the contour plot of the difference between the ferro and antiferro order parameters for (a) and of the chiral current for (b).

We now move to the $\theta = 0$ case, which is represented in Fig. 11(a). In this case, one can readily observe that there is no TCP phase, but that the SSB AFM_x sets in at zero imbalance for vanishingly small interactions. This result is consistent with the qualitative phase diagram of Fig. 2, and has very interesting consequences. While magnetism in standard Hubbard ladders only appears for small superexchange couplings, making its detection with cold atoms rather challenging due to the required temperatures, the AFM_x order in the Creutz-Hubbard ladder for small fluxes appears at much stronger scales, those set by the bare tunneling. This can be a very interesting starting point to introduce a nonzero doping and explore the interplay of magnetism and hole mobility in connection to fermionic mechanisms of superconductivity.

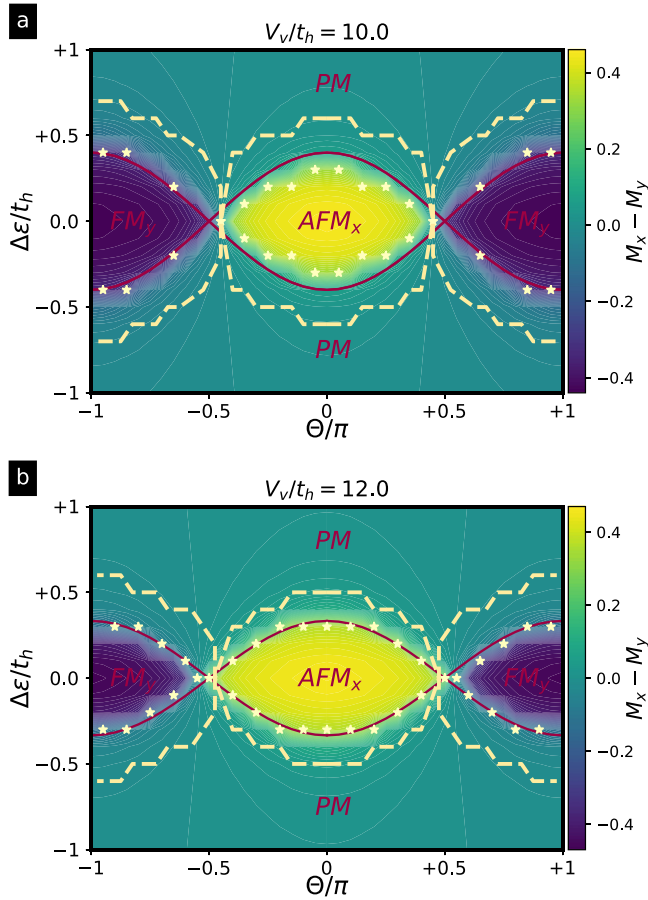


FIG. 12. Phase diagram for strong interactions. (a) $V_v = 10t_h$ and (b) $V_v = 12t_h$. The phase diagram displays a long-range ferromagnetic phase (FM_y), an antiferromagnetic phase (AFM_x), and a paramagnetic phase (PM). The horizontal axis represents the flux, whereas the vertical axis corresponds to the ratio of the energy imbalance to the tunneling strength. The red line shows the transition points Eq. (37) of the effective spin model with D-M interaction in strong coupling limit Eq. (32). The yellow stars show the critical points found by DMRG. Instead, the shaded yellow lines show the critical points from the self-consistently mean-field. The background contour plot represents the difference between the ferro- and antiferro-order parameters.

B. Strong interactions

In Sec. IV B, we introduced an effective spin model Eq. (32) with Dzyaloshinskii-Moriya couplings in the limit of very strong interactions. This model is exactly solvable and allowed us to predict a pair of critical lines Eq. (37) separating the orbital FM_y , AFM_x , and PM. We remark that these predictions are strictly valid in the limit where $V_v/t_h \rightarrow \infty$, and we should explore when these predictions are valid for large, yet finite, interactions. In Fig. 12, we present the ground-state phase diagrams as a function of θ and $\Delta\epsilon$ for two values of the interactions $V_v = 10t_h$ and $V_v = 12t_h$, which correspond to the green- and magenta-shaded planes of the schematic phase diagram of Fig. 2. The red line, in both phase diagrams, represents the analytical critical line Eq. (37), whereas the white stars stand for the DMRG critical points and the yellow dashed lines represent the mean-field predictions. One can

see that the agreement of the strong-coupling critical lines with the DMRG data improves as the Hubbard interactions are increased, whereas the mean-field results overestimate the regions with long-range order. Note also that, by comparing Figs. 12(a) and 12(b), one can see how the PM region grows significantly as the interactions are increased, to the detriment of the long-range ordered phases, which is a consequence of the scaling of the superexchange and Dzyaloshinskii-Moriya couplings Eq. (33) with the inverse of the Hubbard interactions. Let us now discuss in detail how we have characterized these phases and extracted the critical points.

In the background of Fig. 12, we present a contour plot for the difference of the orbital ferromagnetic and antiferromagnetic order parameters. Let us note that, in analogy to the antiferromagnetic case Eq. (45), one can define the orbital ferromagnetic parameter as

$$M_y = \frac{1}{N_s} \sum_j i(\langle c_{j,u}^\dagger c_{j,d} \rangle - \langle c_{j,d}^\dagger c_{j,u} \rangle), \quad (46)$$

which attains nonzero values for a purely imaginary arrangement of bond densities. Note that such an arrangement is reminiscent of a set of alternating fermionic currents that flow vertically between the legs of the ladder. However, in contrast to the circulating chiral current Eq. (19), the corresponding vertical bare tunnelings are absent from the original Hamiltonian Eq. (1), and we would thus lack a continuity equation for such fermionic currents.

To avoid numerical problems due to the incomplete symmetry breaking of the magnetic order parameters M_x, M_y , we instead determine instead the corresponding structure factors

$$S_{T_y T_y}(k) = \frac{1}{N_s^2} \sum_{i,j} e^{ika(i-j)} \langle T_i^y T_j^y \rangle, \quad (47)$$

$$S_{T_x T_x}(k) = \frac{1}{N_s^2} \sum_{i,j} e^{ika(i-j)} \langle |T_i^x T_j^x| \rangle,$$

where the orbital spin operators are defined in Eqs. (31). The zero-momentum component of these structure factors yield the desired magnetizations in the thermodynamic limit $M_y = (S_{T_y T_y}(0))^{1/2}$, $M_x = (S_{T_x T_x}(0))^{1/2}$. In the insets of Figs. 13(a) and 13(c), we show the two M_y, M_x order parameters, which attain a nonzero value for small energy imbalance and for large $\theta = 0.65\pi$ and small $\theta = 0.1\pi$ magnetic fluxes, respectively. To locate the corresponding critical points delimiting the phase boundaries, we calculate the respective susceptibilities $\chi_{M_y} = \partial M_y / \partial \Delta\epsilon$, and $\chi_{M_x} = \partial M_x / \partial \Delta\epsilon$, which again show peaks whose FSS should determine the critical lines accurately. In the main panels of Figs. 13(a) and 13(c), we can see how the susceptibilities peak at symmetric values of the zero-imbalance axis, and how these peaks grow with the lattice size. The numerical results shown in Figs. 13(b) and 13(d) show that the susceptibility peaks agree considerably well with the analytical predictions already for these finite interactions and ladder lengths.

In Fig. 14, we show that the correlated FM_y and AFM_x can still support large chiral currents around the ladder. In fact, the ferromagnetic and antiferromagnetic long-range order phase supports persistent chiral current for small imbalance $\Delta\epsilon$, and it disappears in the orbital magnetic phase. This suggests that

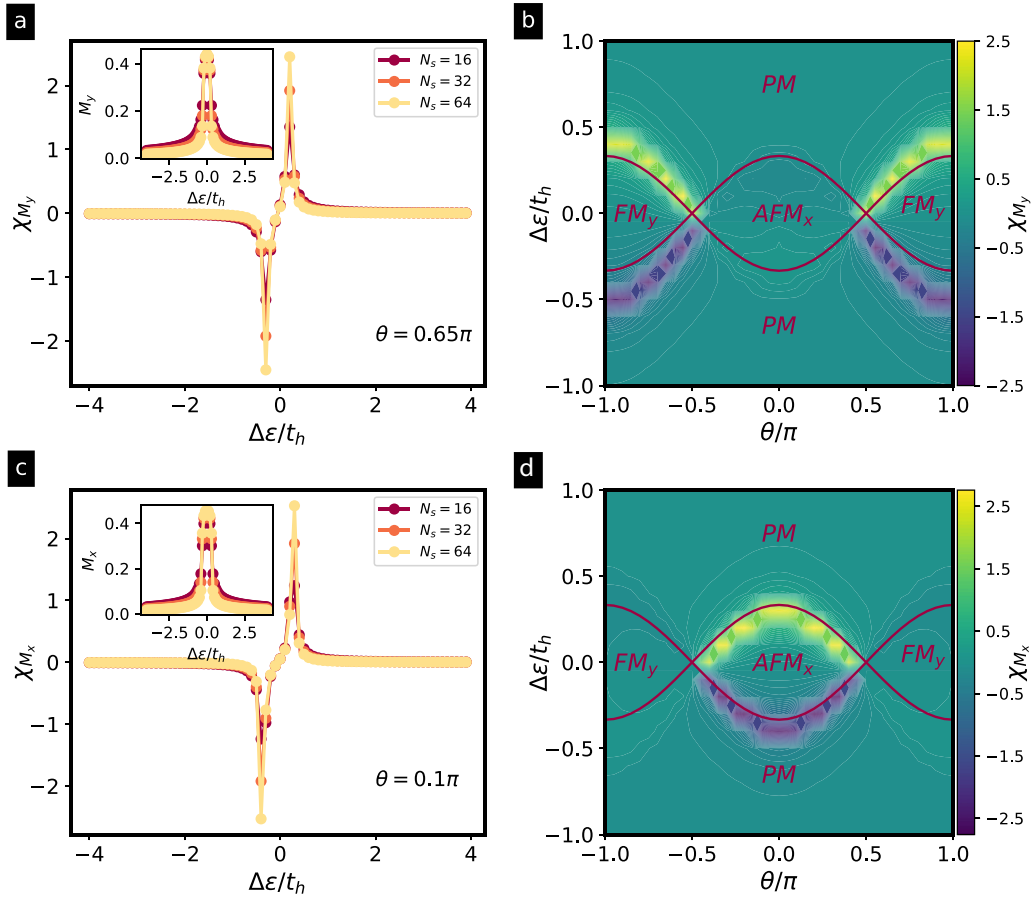


FIG. 13. Magnetic susceptibilities for strong interactions. (a) the divergence of χ_{M_y} with growing system size indicate the phase transition between FM_y and PM phases for a cut of phase diagram at $V_v = 10t_h$ and $\theta = 0.65\pi$. (b) The contour plot of χ_{M_y} for system size $N_s = 64$ distinguishes two FM_y lobes. The red line shows the analytical critical points Eq. (37) of the effective spin model (32), strictly valid for infinitely-large Hubbard interactions. (c) the divergence of χ_{M_x} with growing system size indicates the phase transition between AFM_x and PM phases for $V_v = 10t_h$ and $\theta = 0.1\pi$. (d) The contour plot of χ_{M_x} for system size $N_s = 64$ delimits the AFM_x phase. The red line shows the analytical critical points (37).

the correct indicator for the phase transition FM_y - AFM_x is the chiral susceptibility. Moreover this phenomenon is related to the Chiral Mott insulator phase introduced for quasi-one-dimensional systems [76,171,172] and for two-dimensional systems [173–178]. In Fig. 14(a), we show the numerical results of the chiral current in function of the flux θ for different imbalance interactions. In Fig. 14(b), we present the contour plot of the chiral current. It shows an inversion around the critical line predicted by the Eq. (37). To locate the critical points delimiting the phase boundaries, we calculate the chiral susceptibility χ_c . In Fig. 14(c), we can see how the chiral susceptibility symmetric peaks at symmetry values of the zero- θ axis. Moreover, the numeric results shown in Fig. 14(d) show that the susceptibility peaks agree well with the critical line predicted by Eq. (37) for the FM_y - AFM_x phase transition.

C. Entanglement spectroscopy

Thus far, we have used a conventional condensed-matter approach to characterize the phase diagram of the model, which is based on exploiting currents, susceptibilities, and correlation functions to identify phases with long-range order

or symmetry-protected topological phases. In this section, we follow an alternative approach based on the ground-state entanglement to understand the phase diagram of the model.

Among the various existing measures of entanglement on a bipartite scenario [179], we compute the entanglement spectrum and the entanglement entropy that enjoy a privileged status within the realm of quantum many-body system [180]. With regard to the first one, we define a bipartition of the system and write the ground state as $|\psi_{g.s.}\rangle = \sum_n \lambda_n |\psi_n\rangle_L |\psi_n\rangle_R$, where L and R are two subsystems and $\{\lambda_n\}$ are the corresponding Schmidt coefficients. The entanglement spectrum is defined as the set of all the Schmidt coefficients in logarithmic scale $\epsilon_n = -2 \log(\lambda_n)$, and it can be directly extracted from the MPS calculations. As originally pointed out in Ref. [181], in the context of the characterization of the Haldane phase of Heisenberg-type magnets, the degeneracy of the entanglement spectrum identifies the symmetry-protecting topological phase.

It has been established that the entanglement spectrum is degenerate for symmetry-protected topological phases [170,182,183]. In particular, this degeneracy is robust against symmetric perturbations as long as the many-body gap of the

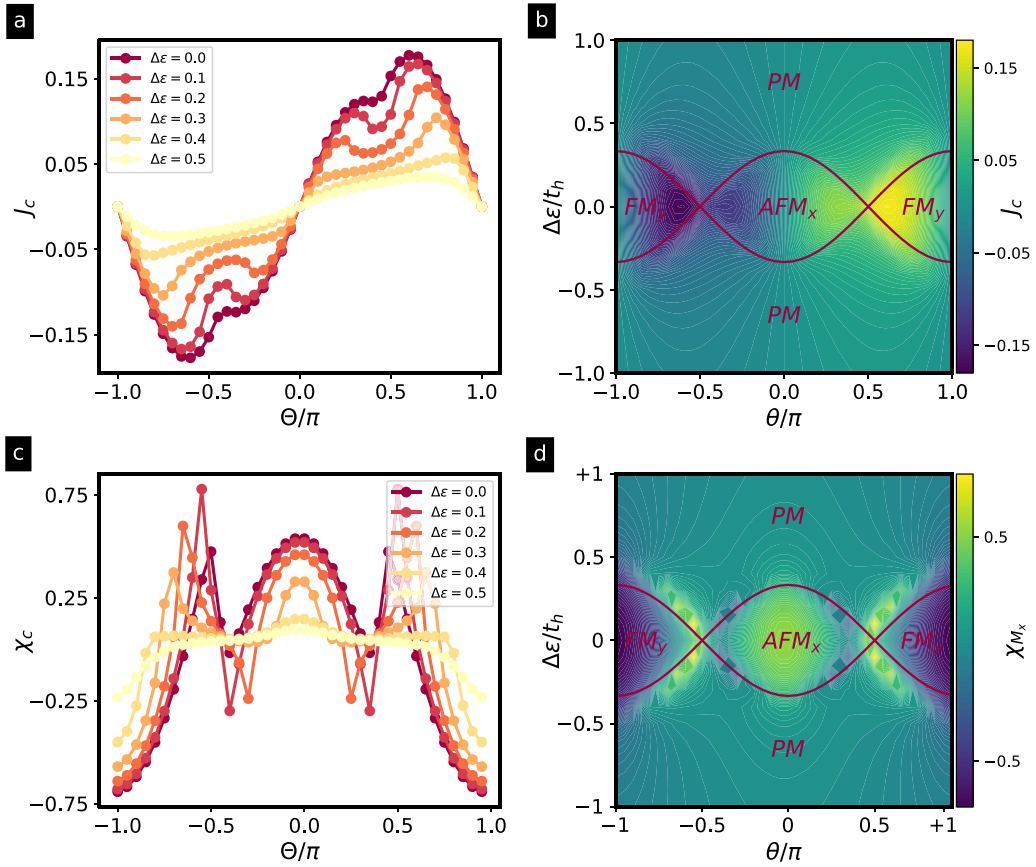


FIG. 14. Chiral flows for strong interactions. (a) Chiral current as a function of the magnetic flux for different energy imbalances $\Delta\epsilon$ and $V_v = 12t_h$. (b) The contour plot of the chiral current qualitatively distinguishes the two phases. The red line shows the transition points of the effective spin model with D-M interaction in strong coupling limit Eq. (32). (c) Divergence of chiral susceptibility for different imbalance $\Delta\epsilon$ that indicates the phase transition between FM_y - AFM_x phases. (d) The maximums of χ_c that delimit the FM_y and AFM_x lobes.

system remains open. In Fig. 15(a), we present the entanglement spectrum degeneracy for the Creutz-Hubbard model in function of $(\theta/\pi, \Delta\epsilon/t_h)$ for different values of interactions

strength V_v . The dark blue region represents the region where the AFM_x and PM are sited and the entanglement spectrum is trivial. Instead, the two lobes represent the TCP phase in which

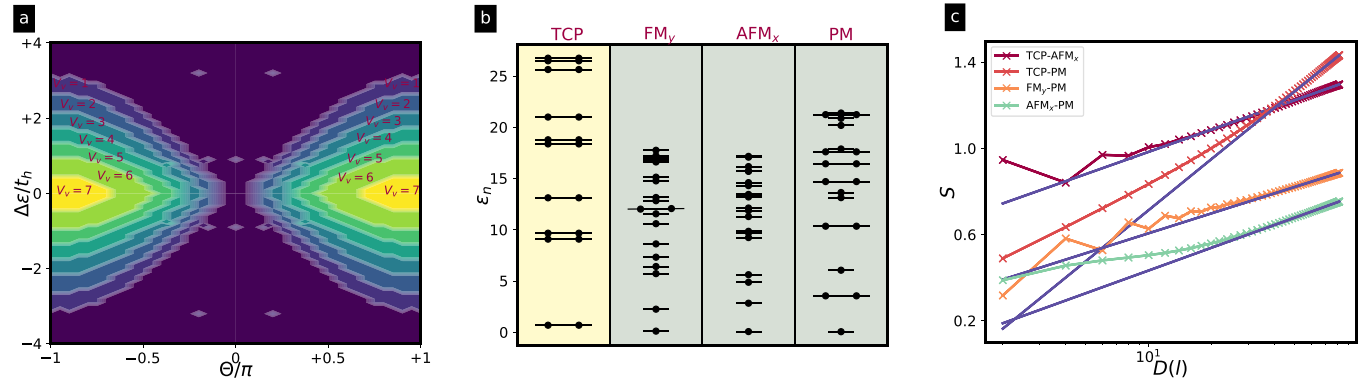


FIG. 15. Entanglement spectrum and entanglement entropy. (a) Degeneracies of the entanglement spectrum in the $(\theta, \Delta\epsilon)$ plane for different interactions. We show that the region in which the entanglement spectrum shows an exact twofold degeneracy, and thus corresponds to the topological crystalline phase, gets reduced by increasing the interactions. (b) Low-lying eigenvalues of the entanglement spectrum for the different phases. For a ladder of length $N_s = 128$, and for a half-chain bipartition of the chain. Only the TCP phase displays an exact twofold degeneracy. (c) Entanglement entropy for l -sites block reduced density matrix ρ_l obtained from a ladder of length $N_s = 128$. The blue, red, and yellow crosses correspond to the data for the critical points. The solid lines correspond to the fittings with the conformal field theory predictions Eq. (49), where c is the central charge. The fitted central charges are $c = 1.02$ (for the TCP-PM transition), $c = 0.503$ (for the TCP- AFM_x transition), $c = 0.49$ (for the FM_y -PM transition), and $c = 0.45$ (for the AFM_x -PM transition), respectively.

the entanglement spectrum is fully degenerate. The effect of the interactions shrinks the two TCP lobes. In fact, as shown in Fig. 15(a), the spectrum degenerate region is reduced. As shown in Fig. 15(b) (yellow column), the entanglement spectrum in the TCP phase is clearly doubly degenerate, whereas in the PM, FM_y , and AFM_x phases, such a degeneracy of all eigenvalues is lost (green columns). This supports our claim about the topological nature of the wide region of the phase diagram labeled as TCP, and demonstrates that the TCP survives to considerable strong interactions. In particular, in the left panel of Fig. 15(b), we present the entanglement spectrum for weak interactions for different values of the imbalance $\Delta\epsilon$ and fluxes θ . We consider a bipartition in the middle of chain, for $\Delta\epsilon = 0$ and $\theta = 0.5\pi$. Increasing $\Delta\epsilon$ and decreasing θ , we enter in the AFM_x or in PM phase, and the entanglement spectrum is trivial and almost completely degenerate, as shown in the green columns.

With regard to the block entanglement entropy, it is defined as

$$S(l) = -\text{Tr}(\rho_l \ln \rho_l), \quad (48)$$

where $\rho_l = \text{Tr}_{N_s-l}(|\epsilon_{g.s.}\rangle\langle\epsilon_{g.s.}|)$ is the reduced density matrix of the left block with l sites for the bipartition of each leg of the ladder of N_s sites. Remarkably enough, not only the block entanglement serve as a probe of criticality due to its divergence at phase transition, but its scaling with system size also reveals the central charge c of the conformal field theory underlying the critical behavior [184–186]. For a critical system with open boundary conditions, the block entanglement entropy scales as

$$S(l) = \frac{c}{6} \ln \left(\frac{2N_s}{\pi} \sin \frac{\pi l}{N_s} \right) + C, \quad (49)$$

where we introduce a nonuniversal constant C . Since such entanglement entropy can be easily recovered from our MPS results, calculating the central charge of the different critical lines of our phase diagram can serve as an additional confirmation of our previous derivations. To explore the scaling region of the quantum phase transition between topological and trivial band insulators, we represent in Fig. 15(c) the critical entanglement entropy as a function of the so-called chord length $D(l, N_s) = (2N_s/\pi) \sin(\pi l/N_s)$, along the critical lines in five representative cases. For the TCP-PM transition, the central charge value agrees with $c = 1$. This result can be understood well in the weakly interesting limit. In this regime, the Creutz-Hubbard model for generic flux can be understood as two coupled Ising chains, as shown in Appendix. In the limit of π flux, the model is mapped to a couple of Ising chains in transverse magnetic field. Accordingly, the corresponding CFT should have central charge of $c = 1/2 + 1/2 = 1$ such that we would expect the scaling $S(l) = (1/6) \ln[(2N_s/\pi) \sin(\pi l/N_s) + a]$. In Fig. 15(c), we also show that predictions are also confirmed for a various fluxes.

For the strongly interacting regime, we showed in previous sections that the FM_y -PM and AFM_x -PM transitions can be accounted for by an XY model with Dzyaloshinskii-Moriya (D-M) interaction. In the limit of $\theta = \pi$, or $\theta = 0$, the model becomes a single Ising model in a transverse field. Accordingly, the corresponding CFT should have a central charge

of $c = 1/2$, and $S(l) = \frac{1}{12} \ln[(\frac{2N_s}{\pi}) \sin(\frac{\pi l}{N_s})] + C$. In contrast to the previous case, the critical phenomena is governed by the CFT of single Majorana fermion with central charge $c = 1/2$.

Finally, in the intermediate interacting regime we argue that the relevant physics to understand the TI-FM phase transition is by approximating a complicated non-SM. In Fig. 15(c), we show the entanglement entropy between the N -physical sites in the original basis and therefore measure $S(l) = \frac{1}{12} \ln[(\frac{2N_s}{\pi}) \sin(\frac{\pi l}{N_s})] + C$ for a system of length N_s with a central charge of $c = 1/2$.

VI. COLD-ATOM RAMAN LATTICE SCHEME

As outlined in the Introduction, despite the fact that laser-cooled gases of neutral atoms move at velocities well below the speed of light [187], these systems yield an ideal platform for the quantum simulation [25] of relativistic QFTs [37]. Following the perspectives of lattice field theories, one need not look for cold-atom quantum simulators directly described by continuum QFTs (15), but instead look for a lattice model with critical points around which a long-wavelength description coincides with the target relativistic QFT. In this section, we describe a scheme based on cold atoms in optical Raman lattices for the quantum simulation of the Creutz-Hubbard ladder under an arbitrary flux (1)-(2). As emphasized previously, such a quantum simulator would provide the first experimental realization of Lorentz-violating terms (16) studied in the context of the SME [4–6], and combined with four-Fermi interactions of the GN type.

We note that the fermionic Creutz ladder has been recently realized in experiments with two-orbital ultracold atoms in shaken optical lattices [188,189]. In principle, interaction effects could be explored by including more hyperfine states. Note, however, that such interacting models would likely correspond to a spin-full version of the Creutz ladder with short-range Hubbard-type interactions [see Fig. 1(e)], which is different from the target model Eqs. (1) and (2). To build the desired quantum simulator, the scheme proposed in Ref. [131] exploits the idea of synthetic dimensions [114] by mapping the ladder legs to a couple of hyperfine atomic states from the ground-state manifold [91,95]. The attractive feature of this scheme is that the interactions along the vertical direction Eq. (2) in Fig. 1(g), the so-called synthetic dimension, are mapped onto contact Hubbard interactions, which are readily implemented by the s -wave scattering of two ultracold atoms trapped in the same site of the optical lattice [71,190].

Synthetic dimensions have been successfully exploited for the quantum simulation of rectangular ladders under a background magnetic field. The associated magnetic flux across the square plaquettes of the ladder can be simulated by a local Raman transition between the two hyperfine states [115,117,118], which induces a Peierls-substituted vertical tunneling that connects the upper and lower legs of the ladder [see Fig. 1(c)]. For the Creutz ladder, the situation is complicated further due to the cross-link nature of the interleg tunnelings [see Fig. 1(g)]. As proposed in Ref. [131], these cross-linked terms could be implemented by a Raman-assisted tunneling scheme [191] that activates a spin-flipping tunneling against the energy penalty of a linear lattice tilt. Note that as the cross-link tunnelings take place in both directions, i.e.,

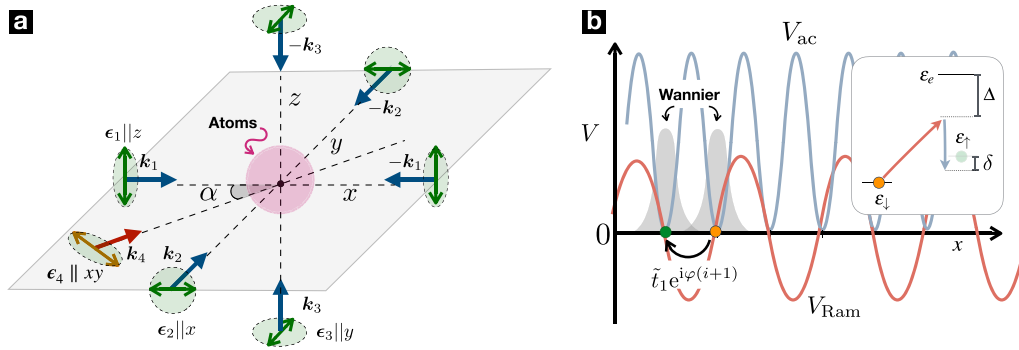


FIG. 16. Scheme of the optical Raman potential for the quantum simulation of the Creutz-Hubbard ladder. (a) A cloud of atoms, represented by a pink shaded sphere, is subjected to three pairs of counterpropagating laser beams with mutually orthogonal polarizations, here depicted with blue arrows, which create a cubic optical lattice. A fourth laser beam, represented by a red arrow, propagates in the xy plane with an angle α with respect to the x axis, sharing the polarization with the standing wave along that axis $\epsilon_4 \parallel \epsilon_1$. The interference of the standing and traveling wave drives a two-photon Raman transition between two hyperfine states when the beat note is tuned close to the resonance of the latter $\Delta\omega = \omega_1 - \omega_4 = \epsilon_f - \epsilon_l - \delta = \omega_0 - \delta$ by virtually populating a highly off-resonant excited state $\delta \ll \omega_0 \ll \Delta$ [see the inset of (b)]. As shown in (b), due to this interference, this Raman term V_{Ram} has a doubled period with respect to the static optical lattice V_{ac} . The atoms trapped at the minima of this optical lattice do not see any intensity of the Raman beams and there is no local transitions. On the other hand, the overlap between neighboring Wannier functions of opposite spin mediated by this Raman potential can lead to a spin-flipping tunneling of strength \tilde{t}_1 with a site-dependent phase φ , which is controlled by the tilting angle α .

(u, i) \rightarrow ($d, i + 1$) and (d, i) \rightarrow ($u, i + 1$), the scheme does not require the use of state-dependent lattices as occurs for the simulation of the Hofstadter model [191], minimizing in this way the expected heating due to residual spontaneous emission in the fermionic Raman couplings. The implementation of the horizontal tunnelings [see Fig. 1(g)] requires a different mechanism to assist the spin-conserving tunneling while imprinting an effective Peierls' phase. In the scheme of Ref. [131], this is provided by an additional shallower lattice potential with a doubled wavelength, the intensity of which is periodically modulated. This allows for a Floquet-assisted tunneling mechanism with the desired Peierls' phase, mimicking the role of the external magnetic flux.

We note that the combination of Floquet-assisted tunneling with Hubbard interactions, as would be required for this full quantum simulator of the Creutz-Hubbard ladder [131], may present limitations due to a heating mechanism where the atoms get excited by resonantly absorbing quanta from the periodically driven radiation [132,192,193]. Although there has been promising progress in the minimization of this heating in specific optical-lattice implementations [194–197], it would be desirable to come up with a different scheme that implements the Peierls phases in the cross-linked geometry. The goal of this section is to present such a scheme.

We show that recent progress in synthetic spin-orbit coupling with cold atoms in so-called optical Raman potentials [42] can be exploited for the full quantum simulator of the Creutz-Hubbard ladder Eqs. (1) and (2). In these schemes, one combines periodic ac-Stark shifts from a standing wave with Raman potentials that stem from the interference of lasers in standing- and traveling-wave configurations. As discussed in more detail below, when the beat note of the standing- and traveling-wave laser beams is tuned close to the spin-flip transition frequency, the Raman cross terms do not drive local spin flips [198–202] but instead assist a spin-flipping tunneling that can be used to simulate spin-orbit coupling [150–153]. Although these Raman schemes may also be limited by resid-

ual photon scattering from the off-resonant excited state, the associated heating is not as severe as that of fermions trapped in state-dependent lattices since, if the available laser intensity is not the limiting factor, this heating can be minimized by working with larger Raman detunings Δ with respect to the excited state [see inset of Fig. 16(b)]. In any case, one may also consider using lanthanide [120,203–205] or alkali-earth [121,122,153] atoms to minimise it further.

Let us now describe in detail how these periodic optical potentials can be exploited for the specific quantum simulation of the Creutz-Hubbard ladder Eqs. (1) and (2), and how to tune the value of the synthetic magnetic flux θ . In contrast to the scheme that realizes Rashba- or Dirac-type spin-orbit coupling [42], we consider a configuration where the traveling wave does not propagate orthogonally to the x -axis standing wave but instead at an angle α [see Fig. 16(a)]. In addition, we consider two additional standing waves with orthogonal polarizations along the remaining spatial directions, which will lead to periodic optical potentials along the y and z axes. In the regime where the lasers are far detuned with respect to an excited state, this creates a periodic optical potential for the atoms in two hyperfine states $\sigma \in \{\uparrow, \downarrow\}$, namely,

$$V = \sum_{\alpha} \frac{V_{0,\alpha}}{2} \cos^2(\mathbf{k}_{\alpha} \cdot \mathbf{x}) \mathbb{I}_2 + \frac{\tilde{V}_0}{2} \cos(\mathbf{k}_1 \cdot \mathbf{x}) e^{i(k_4 x - \Delta \omega t)} \sigma^+ + \text{H.c.}, \quad (50)$$

where $\sigma^+ = |\uparrow\rangle \langle \downarrow|$. Here, $V_{0,\alpha}$ are the amplitudes of the ac-Stark shifts induced by pairs of counterpropagating laser beams along each of the axes $\mathbf{k}_{\alpha} = k_{\alpha} \mathbf{e}_{\alpha}$ with $\alpha \in \{1, 2, 3\} \equiv \{x, y, z\}$. These pairs of laser beams have mutually orthogonal polarizations, such that the interference patterns along each axis in the first term of Eq. (50) can be tuned independently, and thus correspond to a standard cubic optical lattice. Additionally, \tilde{V}_0 is the amplitude of the two-photon Raman transition, whereby the spin state gets flipped by virtually

populating an excited state. As shown in the inset of Fig. 16(b), this transition involves absorbing a photon from the traveling wave, which propagates along $\mathbf{k}_4 = k_4 \cos \alpha \mathbf{e}_1 + k_4 \sin \alpha \mathbf{e}_2$, and subsequently reemitting it in the standing wave. This leads to a beat note of frequency $\Delta\omega = \omega_4 - \omega_1$ that can drive the spin flips when tuned close to the resonance $\Delta\omega \approx \omega_0$. A crucial aspect of these types of schemes, which can already be appreciated at this stage, is that the period of the spin-flipping potential is doubled with respect to that of the static optical lattice [see Fig. 16(b)]. As such, the atoms residing at the minima of the latter do not see any Raman intensity that would drive local transitions but it is only in the spin-flip tunneling where this Raman term contributes.

As noted at the beginning of this section, these systems can be described by the following nonrelativistic QFT:

$$H = \int d^3x \sum_{\sigma, \sigma'} \Phi_{\sigma'}^{\dagger}(\mathbf{x}) \left(-\frac{\nabla^2}{2m} + \langle \sigma | V(\mathbf{x}) | \sigma' \rangle \right) \Phi_{\sigma}(\mathbf{x}) + \int d^3x \int d^3x' \sum_{\sigma, \sigma'} \Phi_{\sigma}^{\dagger}(\mathbf{x}) \Phi_{\sigma'}^{\dagger}(\mathbf{x}') \frac{2\pi a_s}{m} \times \delta(\mathbf{x} - \mathbf{x}') \Phi_{\sigma'}(\mathbf{x}') \Phi_{\sigma}(\mathbf{x}), \quad (51)$$

where m is the mass of the atoms, and a_s the s -wave scattering length for the low-energy two-body collisions. We have introduced the fermionic field operators $\Phi_{\sigma}^{\dagger}(\mathbf{x})$, $\Phi_{\sigma}(\mathbf{x})$ that create-annihilate an atom at position \mathbf{x} with internal state σ . Note that these fields differ from the relativistic ones Eq. (10), which will be recovered in the long-wavelength limit of the lattice model. To obtain such a lattice description, we consider the regime of deep optical lattices $V_{0,\alpha} \gg E_{R,\alpha} = k_{\alpha}^2/2m$, where the atoms are tightly confined to the minima of the periodic blue-detuned optical lattice [see Fig. 16(b)]. The lattice sites thus correspond to $\mathbf{x}_i^0 = \sum_{\alpha} \frac{\lambda_{\alpha}}{2} (i_{\alpha} + \frac{1}{2}) \mathbf{e}_{\alpha}$, where $\lambda_{\alpha} = 2\pi/k_{\alpha}$ are the wavelengths of the standing-wave laser beams, and $i_{\alpha} \in \mathbb{Z}_{N_{\alpha}}$. We now express the fields in the Wannier basis

$$\Phi_{\sigma}(\mathbf{x}) = \sum_i w(\mathbf{x} - \mathbf{x}_i^0) f_{i,\sigma}, \quad \Phi_{\sigma}^{\dagger}(\mathbf{x}) = \sum_i w(\mathbf{x} - \mathbf{x}_i^0) f_{i,\sigma}^{\dagger}, \quad (52)$$

where $w(\mathbf{x} - \mathbf{x}_i^0)$ are the Wannier functions localized around each minima \mathbf{x}_i^0 of the optical potential and $f_{i,\sigma}^{\dagger}$, $f_{i,\sigma}$ is a set of dimensionless lattice operators that describe the creation-annihilation of fermions in the lowest band of the optical lattice. Substituting these expressions in the QFT Eq. (51), one obtains a lattice model with parameters that depend on the overlaps of these Wannier functions. These parameters decay exponentially fast with the distance and are typically restricted to on-site and nearest-neighbor terms [71,190].

This lattice model is composed of spin-conserving terms

$$H_{\text{sc}} = \sum_i \left(\sum_{\sigma, \alpha} (-t_{\alpha} f_{i,\sigma}^{\dagger} f_{i+\mathbf{e}_{\alpha},\sigma} + \text{H.c.}) + \sum_{\sigma \neq \sigma'} \frac{U_{\uparrow\downarrow}}{2} n_{i,\sigma} n_{i,\sigma'} \right), \quad (53)$$

where $n_{i,\sigma} = f_{i,\sigma}^{\dagger} f_{i,\sigma}$, and we have introduced the tunnelings

$$t_{\alpha} = \frac{4}{\sqrt{\pi}} E_R \left(\frac{V_{0,\alpha}}{E_R} \right)^{\frac{3}{4}} e^{-2\sqrt{\frac{V_{0,\alpha}}{E_R}}}, \quad (54)$$

assuming that the standing waves have the same wavelength $\lambda_{\alpha} = 2\pi/k_{\alpha} = 2\pi/k$, $\forall \alpha$ and $E_R = E_{R,\alpha}$, $\forall \alpha$. Likewise, the Hubbard interaction reads

$$U_{\uparrow\downarrow} = \sqrt{\frac{8}{\pi}} k a_s E_R \left(\frac{V_{0,1} V_{0,2} V_{0,3}}{E_R^3} \right)^{\frac{1}{4}}. \quad (55)$$

By setting $V_{0,2}, V_{0,3} \gg V_{0,1} \gg E_R$, the tunnelings along the y and z axes Eq. (54) are inhibited $t_2, t_3 \ll t_1$, and we obtain an effective Fermi-Hubbard model in one spatial dimension. Note that, in addition to these spin-conserving terms, there will also be local terms corresponding to on-site energies that can be approximated by an overall quadratic trapping potential.

In addition to these contributions, we have the spin-flipping Raman potential Eq. (50) that stems from the interference of the standing and traveling waves along the x axis and will lead to spin-flipping terms in the lattice model. In this case, the local terms are not simply an on-site potential, as discussed in the previous paragraph but instead describe processes where an atom tightly confined to a minimum of the optical potential experiences a Raman transition that flips its internal state $|\uparrow\rangle \leftrightarrow |\downarrow\rangle$. This type of term can indeed be exploited to implement the synthetic dimensions discussed in the Introduction [115,117,118]. Note that these terms correspond to a vertical tunneling within the synthetic ladder and would thus spoil the cross-linked nature of the Creutz-ladder of Fig. 1(g). Fortunately, the corresponding Wannier integrals vanish since the Raman potential is odd with respect to each lattice site while the Wannier functions are even [see Fig. 16(b)]:

$$\int d^3x w(\mathbf{x} - \mathbf{x}_i^0) \frac{\tilde{V}_0}{2} \cos(\mathbf{k}_1 \cdot \mathbf{x}) e^{ik_4 x} w(\mathbf{x} - \mathbf{x}_i^0) = 0. \quad (56)$$

The leading spin-flipping terms are thus described by tunnelings along the x axis that stem from the following overlaps:

$$\int d^3x w(\mathbf{x} - \mathbf{x}_i^0) \frac{\tilde{V}_0}{2} \cos(\mathbf{k}_1 \cdot \mathbf{x}) e^{ik_4 x} w(\mathbf{x} - \mathbf{x}_j^0) \approx \frac{\tilde{V}_0}{2} e^{-\frac{1}{4}mv|\mathbf{x}_i^0 - \mathbf{x}_j^0|^2} \times \cos\left(\frac{1}{2}\mathbf{k}_1 \cdot (\mathbf{x}_i^0 + \mathbf{x}_j^0)\right) e^{\frac{i}{2}k_4(\mathbf{x}_i^0 + \mathbf{x}_j^0)}, \quad (57)$$

where we have performed a Gaussian approximation around the minima of each lattice site, where the lattice potential can be approximated by a harmonic oscillator of frequency $\nu = 2\sqrt{V_{0,1}E_R}$. As occurs for the spin-conserving terms, these tunnelings decay rapidly with the distance, such that we can restrict to nearest neighbors. In this case, the overlaps display a crucial alternation of the sign, $\cos(\frac{1}{2}\mathbf{k}_1 \cdot (\mathbf{x}_i^0 + \mathbf{x}_{i+\mathbf{e}_1}^0)) = \exp\{i\pi(i_1 + 1)\}$, which has been exploited to simulate synthetic spin-orbit coupling [150–152]. The uniqueness of our scheme is that the nonorthogonal propagation of the traveling wave shown in Fig. 16(a) allows us to pick up an arbitrary phase factor that shall also play a crucial role, namely, $\exp\{\frac{i}{2}\mathbf{k}_4 \cdot (\mathbf{x}_i^0 + \mathbf{x}_{i+\mathbf{e}_1}^0)\} = \exp\{i\tilde{\eta}(i_1 + 1)\}$, where

$$\tilde{\eta} = \frac{k_4}{k_1} \cos \alpha. \quad (58)$$

Note that there is also a dependence of this phase factor on the particular lattice site along the y axis, but the negligible tunnelings along this direction allow us to gauge it away without changing the dynamics.

Let us now tune the Raman beat note slightly of resonance with respect to the internal transition $\Delta\omega = \omega_0 - \delta$, where the detuning is constrained to $\delta \ll \omega_0$. Considering the discussion in the previous paragraph and working in a rotating frame, we find that the Raman potential leads to the following spin-flipping tunnelings and energy imbalance:

$$H_{\text{sf}} = \sum_i \tilde{t}_1 (e^{i\varphi(i+1)} f_{i,\uparrow}^\dagger f_{i+\mathbf{e}_1,\downarrow} + e^{-i\varphi(i+1)} f_{i,\downarrow}^\dagger f_{i+\mathbf{e}_1,\uparrow}) + \text{H.c.} \\ + \sum_i \frac{\delta}{2} (f_{i,\uparrow}^\dagger f_{i,\uparrow} - f_{i,\downarrow}^\dagger f_{i,\downarrow}), \quad (59)$$

where we have introduced the following parameters:

$$\tilde{t}_1 = \frac{\tilde{V}_0}{2} e^{-\frac{\pi^2}{4} \sqrt{\frac{V_{0,1}}{E_R}}}, \quad \varphi = \pi(1 + \tilde{\eta}). \quad (60)$$

The final step to define our quantum simulator is to map the fermionic operators of the Creutz-Hubbard ladder Eqs. (1) and (2) via a synthetic dimension to the cold-atom operators,

$$c_{i,u} = e^{-i\frac{\varphi}{2}(i+1)} f_{i,\uparrow}, \quad c_{i,d} = e^{+i\frac{\varphi}{2}i} f_{i,\downarrow}, \quad (61)$$

such that the cold-atom lattice model in Eqs. (53)–(59) maps directly onto the Creutz-Hubbard ladder Eq. (1) and (2) with the following identification of microscopic parameters:

$$t_h = t_1, \quad t_d = -\tilde{t}_1, \quad \Delta\epsilon = \delta, \quad \theta = \varphi, \quad V_v = U_{\uparrow\downarrow}. \quad (62)$$

Note that the various observables discussed in our study of the Creutz-Hubbard ladder may be modified by virtue of the $U(2)$ gauge transformation Eqs. (61). One should thus identify the correct cold-atom operators that contain the relevant information about the ground-state phases of the Creutz-Hubbard ladder.

It follows from our discussion that all of these parameters can be tuned independently. The horizontal tunneling is controlled by the intensity of the standing-wave lasers via Eq. (54). If, on the other hand, one modifies the intensity of the traveling-wave laser, only the spin-flip tunneling will change Eqs. (60), which translates into a modification of the cross-link tunneling of the Creutz-Hubbard ladder [see Fig. 1(g)]. To modify the synthetic magnetic flux independently, Eqs. (58)–(60) show that one must either modify the angle α of propagation of the traveling wave. Similarly, the energy imbalance is controlled by the beat-note detuning, which can be readily modified by changing the frequency of traveling-wave laser. Finally, the Hubbard interactions can be tuned by exploiting a Feshbach resonance in the scattering length Eq. (55).

VII. CONCLUSIONS AND OUTLOOK

In this paper, we have described the connection between Lorentz-violating four-Fermi QFTs and models of correlated TCPs. By focusing on the Creutz-Hubbard ladder for arbitrary magnetic flux, we have presented a thorough analysis based on analytical and numerical tools, showing that, as a consequence of the violation of Lorentz invariance, persistent

chiral currents can coexist with strong correlations in the topological crystalline phase. We have discussed in detail the phase diagram of the model and the nature of the phase transitions, showing that the chiral current and its susceptibility provide relevant information, which can be complemented with other observables and entanglement-related quantities. We have also discussed an experimental scheme based on ultracold Fermi gases in tilted Raman lattices for the quantum simulation of these phenomena. We refer the reader again to Sec. II C, where all results have been summarized. We would like to conclude by noting that our paper constitutes an example of the useful dialogue and exchange of ideas between the high-energy physics, condensed matter, quantum information, and quantum optics, hopefully stimulating further cross-disciplinary efforts in the future. From the above results, we are convinced that the synthetic Creutz-Hubbard ladder with generic flux can become a work horse in the theoretical and experimental study of correlated topological phases of matter, connecting high-energy physics and condensed matter, and proving a clear path to for its implementation via ultracold atoms. This would provide an experimental realization of Lorentz-violating QFTs within the SME.

As an outlook, it would be very interesting to exploit these cross-disciplinary approaches to understand the physics of the Creutz-Hubbard ladder at generic flux, and thus the GNME, as one moves away from half filling and thus explores finite fermion densities in the continuum QFT. It would also be interesting to explore real-time dynamical effects in this model, in particular, in connection with anomalies, the circulating chiral current and the underlying violation of Lorentz symmetry. This would require us to upgrade flux θ to a dynamical variable with its own dynamics described by a $U(1)$ lattice gauge theory, following a similar gauging as in the case of a \mathbb{Z}_2 gauge group [206]. As discussed for other lattice models in Refs. [207,208], \mathbb{Z}_N discrete gauge groups could also be explored as a proxy for the $U(1)$ ladder gauge theory. It would be very interesting to study the interplay of this gauge theory with the topological crystalline insulator and its associated edge states. We note that both the finite-density and real-time phenomena provide very challenging problems where the advantage of the quantum simulator could be exploited. Finally, it would also be interesting to explore how other terms within the SME can be incorporated in a lattice model, and how this model could be realized in experiments of ultracold atoms.

ACKNOWLEDGMENTS

M.L. group acknowledges support from ERC AdG NOQIA; Agencia Estatal de Investigación (R&D Project No. CEX2019-000910-S, funded by No. MCIN/AEI/10.13039/501100011033, Plan National FIDEUA No. PID2019-106901GB-I00, FPI, QUANTERA MAQS No. PCI2019-111828-2, Proyectos de I + D + I Retos Colaboración No. RTC2019-007196-7); Fundació Cellex; Fundació Mir-Puig; Generalitat de Catalunya through the CERCA program, AGAUR Grant No. 2017 SGR 134, QuantumCAT No. U16-011424, cofunded by ERDF Operational Program of Catalonia; EU Horizon 2020 FET-OPEN OPTOLogic (Grant No 899794); National Science Centre, Poland (Symfonia Grant No. 2016/20/W/ST4/00314);

Marie Skłodowska-Curie STREDCH Grant. No. 101029393; La Caixa Junior Leaders fellowships (No. ID100010434) and EU Horizon 2020 under Marie Skłodowska-Curie Grant Agreement No. No 847648 (No. LCF/BQ/PI19/11690013, No. LCF/BQ/PI20/11760031, No. LCF/BQ/PR20/11770012, and No. LCF/BQ/PR21/11840013). A.B. acknowledges support from the Ramón y Cajal Program No. RYC-2016-20066, CAM/FEDER Project No. S2018/TCS-4342 (QUITEMADCM), and No. PGC2018-099169-B-I00 (MCIU/AEI/FEDER, UE).

APPENDIX: WEAK INTERACTIONS AND COUPLED ISING CHAINS

In this Appendix, we discuss more in detail the weak interacting limit $t_h \gg V_v$ of the Creutz-Hubbard ladder for generic flux, and in particular we will show how in this limit we can map the Creutz ladder as spin ladder.

We start from the free part of the Creutz-Hubbard Hamiltonian H_c defined in Eq. (1). Introducing the spinor notation and performing the transformation $c_j = (-i\sigma_z)^j \tilde{c}_j$, we obtain that the hopping along the two legs becomes now identical at the price of having site-dependent diagonal hopping terms that connect neighboring sites in opposite legs of the ladder:

$$H_c = \sum_j \tilde{c}_j^\dagger \left[-t_h I - t_d \cos\left(\frac{\theta}{2}(2j+1)\right) \sigma_x + t_d \sin\left(\frac{\theta}{2}(2j+1)\right) \sigma_y \right] c_{j+1} + \frac{\Delta\epsilon}{4} \tilde{c}_j^\dagger \sigma_z \tilde{c}_j + \text{H.c.} \quad (\text{A1})$$

Introducing the following rung operators:

$$\begin{aligned} \hat{r}_{j,1} &= \frac{i^j}{\sqrt{2}} [i\tilde{c}_{j,u} + (-1)^j \tilde{c}_{j,d}^\dagger], \\ \hat{r}_{j,2} &= \frac{i^j}{\sqrt{2}} [\tilde{c}_{j,u} + (-1)^j \tilde{c}_{j,d}^\dagger], \end{aligned} \quad (\text{A2})$$

Under this canonical transformation, the Hamiltonian is transformed onto

$$H_c = \sum_{jn} \left[-t_h (\hat{r}_{j+1,n}^\dagger \hat{r}_{j,n} + \text{H.c.}) + t_d ((-1)^{j+1} i e^{i\frac{\theta}{2}(2j+1)} \hat{r}_{j+1,n}^\dagger \hat{r}_{j,n}^\dagger + \text{H.c.}) + \frac{\Delta\epsilon}{4} (2\hat{r}_{j,n}^\dagger \hat{r}_{j,n} - 1) \right] \quad (\text{A3})$$

In this particle-hole rung basis Eq. (A2), we identify two independent subsystems which no longer display particle number conservation, but instead have parity conservation. A Jordan-Wigner transformation [209], namely,

$$\hat{r}_{j,n}^\dagger = \Pi_{i<j} (-\sigma_{i,n}^z) \sigma_{j,n}^+ = (\hat{r}_{j,n})^\dagger \quad (\text{A4})$$

reveals the Ising nature of the two subsystems, and leads to a Hamiltonian that can be understood as a two-leg quantum spin ladder

$$H_c = \sum_{jn} \left[-t_h (\sigma_{j+1,n}^+ \sigma_{j,n}^- + \text{H.c.}) + t_d ((-1)^{j+1} i e^{i\frac{\theta}{2}(2j+1)} \sigma_{j+1,n}^+ \sigma_{j,n}^+ + \text{H.c.}) + \frac{\Delta\epsilon}{4} \sigma_{j,n}^z \right]. \quad (\text{A5})$$

We now consider the model with Hubbard-like interactions for the first time. In particular, we take a look at the regime of small interactions $V_v < t$ and study how these interactions alter the results of the non-interacting model. Applying the series of transformations presented above we obtain that the interaction term reads

$$\begin{aligned} \hat{H}_{\text{Hub}} &= \frac{V_v}{2} \sum_j (\hat{r}_{j,1}^\dagger \hat{r}_{j,1} + \hat{r}_{j,2}^\dagger \hat{r}_{j,2} + i \hat{r}_{j,1}^\dagger \hat{r}_{j,2} \\ &\quad - i \hat{r}_{j,2}^\dagger \hat{r}_{j,1} - 2 \hat{r}_{j,1}^\dagger \hat{r}_{j,1} \hat{r}_{j,2}^\dagger \hat{r}_{j,2}). \end{aligned} \quad (\text{A6})$$

For half filling we have $\langle \hat{r}_{j,1}^\dagger \hat{r}_{j,2} - \hat{r}_{j,2}^\dagger \hat{r}_{j,1} \rangle = 0$, simplifying the Hamiltonian to

$$\hat{H}_{\text{Hub}} = \frac{V_v}{2} \sum_j (\hat{r}_{j,1}^\dagger \hat{r}_{j,1} + \hat{r}_{j,2}^\dagger \hat{r}_{j,2} - \hat{r}_{j,1}^\dagger \hat{r}_{j,1} \hat{r}_{j,2}^\dagger \hat{r}_{j,2}). \quad (\text{A7})$$

The Jordan-Wigner transformation translates this expression to a ferromagnetic coupling between the two spin models:

$$\hat{H}_{\text{Hub}} = \frac{V_v}{4} \sum_j (1 - \sigma_{j,1}^z \sigma_{j,2}^z). \quad (\text{A8})$$

In π -flux regime, the imbalanced Creutz-Hubbard model can be understood as two coupled quantum Ising chains. For weak interactions $V_v < t_h$, we can treat the mutual effect of chains on each other through an MF decoupling which renormalizes the original transverse magnetization term.

- [1] M. E. Peskin and D. V. Schroeder, *An Introduction to Quantum Field Theory* (Addison-Wesley, Reading, USA, 1995).
 [2] V. A. Kostelecký and S. Samuel, *Phys. Rev. D* **39**, 683 (1989).
 [3] S. M. Carroll, J. A. Harvey, V. A. Kostelecký, C. D. Lane, and T. Okamoto, *Phys. Rev. Lett.* **87**, 141601 (2001).
 [4] D. Colladay and V. A. Kostelecký, *Phys. Rev. D* **58**, 116002 (1998).

- [5] V. A. Kostelecký, C. D. Lane, and A. G. M. Pickering, *Phys. Rev. D* **65**, 056006 (2002).
 [6] D. Colladay and V. Kostelecký, *Phys. Lett. B* **511**, 209 (2001).
 [7] D. Mattingly, *Living Rev. Relativity* **8**, 5 (2005).
 [8] T. Pruttivarasin, M. Ramm, S. G. Porsev, I. I. Tupitsyn, M. S. Safronova, M. A. Hohensee, and H. Häffner, *Nature (London)* **517**, 592 (2015).
 [9] S. Chadha and H. Nielsen, *Nucl. Phys. B* **217**, 125 (1983).

- [10] E. Fradkin, *Field Theories of Condensed Matter Physics*, 2nd ed. (Cambridge University Press, Cambridge, 2013).
- [11] L. Landau, *Zh. Eksp. Teor. Fiz.* **11**, 26 (1937).
- [12] K. G. Wilson and J. Kogut, *Phys. Rep.* **12**, 75 (1974).
- [13] R. Shankar, *Rev. Mod. Phys.* **66**, 129 (1994).
- [14] J. Bardeen, L. N. Cooper, and J. R. Schrieffer, *Phys. Rev.* **106**, 162 (1957).
- [15] Y. Nambu and G. Jona-Lasinio, *Phys. Rev.* **122**, 345 (1961).
- [16] Y. Nambu and G. Jona-Lasinio, *Phys. Rev.* **124**, 246 (1961).
- [17] P. W. Anderson, *Phys. Rev.* **130**, 439 (1963).
- [18] F. Englert and R. Brout, *Phys. Rev. Lett.* **13**, 321 (1964).
- [19] P. W. Higgs, *Phys. Rev. Lett.* **13**, 508 (1964).
- [20] A. H. Castro Neto, F. Guinea, N. M. R. Peres, K. S. Novoselov, and A. K. Geim, *Rev. Mod. Phys.* **81**, 109 (2009).
- [21] N. P. Armitage, E. J. Mele, and A. Vishwanath, *Rev. Mod. Phys.* **90**, 015001 (2018).
- [22] X.-L. Qi and S.-C. Zhang, *Rev. Mod. Phys.* **83**, 1057 (2011).
- [23] I. Bloch, J. Dalibard, and S. Nascimbène, *Nat. Phys.* **8**, 267 (2012).
- [24] R. Blatt and C. F. Roos, *Nat. Phys.* **8**, 277 (2012).
- [25] R. P. Feynman, *Int. J. Theor. Phys.* **21**, 467 (1982).
- [26] L. Tarruell, D. Greif, T. Uehlinger, G. Jotzu, and T. Esslinger, *Nature (London)* **483**, 302 (2012).
- [27] L. Duca, T. Li, M. Reitter, I. Bloch, M. Schleier-Smith, and U. Schneider, *Science* **347**, 288 (2015).
- [28] C. Schweizer, F. Grusdt, M. Berngruber, L. Barbiero, E. Demler, N. Goldman, I. Bloch, and M. Aidelsburger, *Nat. Phys.* **15**, 1168 (2019).
- [29] A. Mil, T. V. Zache, A. Hegde, A. Xia, R. P. Bhatt, M. K. Oberthaler, P. Hauke, J. Berges, and F. Jendrzejewski, *Science* **367**, 1128 (2020).
- [30] F. M. Surace, P. P. Mazza, G. Giudici, A. Lerose, A. Gambassi, and M. Dalmonte, *Phys. Rev. X* **10**, 021041 (2020).
- [31] B. Yang, H. Sun, R. Ott, H.-Y. Wang, T. V. Zache, J. C. Halimeh, Z.-S. Yuan, P. Hauke, and J.-W. Pan, *Nature* **587**, 392 (2020).
- [32] R. Gerritsma, G. Kirchmair, F. Zähringer, E. Solano, R. Blatt, and C. F. Roos, *Nature (London)* **463**, 68 (2010).
- [33] R. Gerritsma, B. P. Lanyon, G. Kirchmair, F. Zähringer, C. Hempel, J. Casanova, J. J. García-Ripoll, E. Solano, R. Blatt, and C. F. Roos, *Phys. Rev. Lett.* **106**, 060503 (2011).
- [34] E. A. Martinez, C. A. Muschik, P. Schindler, D. Nigg, A. Erhard, M. Heyl, P. Hauke, M. Dalmonte, T. Monz, P. Zoller, and R. Blatt, *Nature (London)* **534**, 516 (2016).
- [35] E. Zohar, J. I. Cirac, and B. Reznik, *Rep. Prog. Phys.* **79**, 014401 (2016).
- [36] M. Dalmonte and S. Montangero, *Contemp. Phys.* **57**, 388 (2016).
- [37] M. C. Bañuls, R. Blatt, J. Catani, A. Celi, J. I. Cirac, M. Dalmonte, L. Fallani, K. Jansen, M. Lewenstein, S. Montangero, C. A. Muschik, B. Reznik, E. Rico, L. Tagliacozzo, K. V. Acoleyen, F. Verstraete, U. J. Wiese, M. Wingate, J. Zakrzewski, and P. Zoller, *European Phys. J. D* **74**, 165 (2020).
- [38] M. Aidelsburger, L. Barbiero, A. Bermudez, T. Chanda, A. Dauphin, D. González-Cuadra, P. R. Grzybowski, S. Hands, F. Jendrzejewski, J. Jünemann, G. Juzeliunas, V. Kasper, A. Piga, S.-J. Ran, M. Rizzi, G. Sierra, L. Tagliacozzo, E. Tirrito, T. V. Zache, J. Zakrzewski *et al.*, *Philos. Trans. R. Soc. A* **380**, 20210064 (2022).
- [39] N. Klco, A. Roggero, and M. J. Savage, *Rep. Prog. Phys.* **85**, 064301 (2022).
- [40] V. A. Kostelecký and N. Russell, *Rev. Mod. Phys.* **83**, 11 (2011).
- [41] V. Galitski and I. B. Spielman, *Nature (London)* **494**, 49 (2013).
- [42] L. Zhang, X.-J. Liu, Spin-orbit coupling and topological phases for ultracold atoms, in *Synthetic Spin-Orbit Coupling in Cold Atoms* (World Scientific, 2018), pp. 1–87.
- [43] E. Dagotto, *Rep. Prog. Phys.* **62**, 1525 (1999).
- [44] E. Dagotto and T. M. Rice, *Science* **271**, 618 (1996).
- [45] G. Sierra, *J. Phys. A: Math. Gen.* **29**, 3299 (1996).
- [46] F. Haldane, *Phys. Lett. A* **93**, 464 (1983).
- [47] I. Affleck, *Nucl. Phys. B* **257**, 397 (1985).
- [48] P. W. Anderson, *Phys. Rev.* **79**, 350 (1950).
- [49] J. Hubbard, *Proc. R. Soc. London, Ser. A* **276**, 238 (1963).
- [50] M. Fabrizio, *Phys. Rev. B* **48**, 15838 (1993).
- [51] L. Balents and M. P. A. Fisher, *Phys. Rev. B* **53**, 12133 (1996).
- [52] H.-H. Lin, L. Balents, and M. P. A. Fisher, *Phys. Rev. B* **58**, 1794 (1998).
- [53] H.-H. Lin, L. Balents, and M. P. A. Fisher, *Phys. Rev. B* **56**, 6569 (1997).
- [54] T. Giamarchi, *Quantum Physics in One Dimension*, International Series of Monographs on Physics, 12 (Clarendon Press, Oxford, 2004).
- [55] R. Noack, S. White, and D. Scalapino, *Physica C: Superconductivity* **270**, 281 (1996).
- [56] S. R. White, R. M. Noack, and D. J. Scalapino, *Phys. Rev. Lett.* **73**, 886 (1994).
- [57] S. R. White, *Phys. Rev. Lett.* **69**, 2863 (1992).
- [58] U. Schollwöck, *Rev. Mod. Phys.* **77**, 259 (2005).
- [59] K. v. Klitzing, G. Dorda, and M. Pepper, *Phys. Rev. Lett.* **45**, 494 (1980).
- [60] D. C. Tsui, H. L. Stormer, and A. C. Gossard, *Phys. Rev. Lett.* **48**, 1559 (1982).
- [61] R. Peierls, *Z. Phys.* **80**, 763 (1933).
- [62] G. Roux, E. Orignac, S. R. White, and D. Poilblanc, *Phys. Rev. B* **76**, 195105 (2007).
- [63] B. N. Narozhny, S. T. Carr, and A. A. Nersesyan, *Phys. Rev. B* **71**, 161101(R) (2005).
- [64] S. T. Carr, B. N. Narozhny, and A. A. Nersesyan, *Phys. Rev. B* **73**, 195114 (2006).
- [65] R. Jackiw and C. Rebbi, *Phys. Rev. D* **13**, 3398 (1976).
- [66] W. P. Su, J. R. Schrieffer, and A. J. Heeger, *Phys. Rev. Lett.* **42**, 1698 (1979).
- [67] R. Jackiw and J. Schrieffer, *Nucl. Phys. B* **190**, 253 (1981).
- [68] M. Atala, M. Aidelsburger, M. Lohse, J. T. Barreiro, B. Paredes, and I. Bloch, *Nat. Phys.* **10**, 588 (2014).
- [69] M. E. Tai, A. Lukin, M. Rispoli, R. Schittko, T. Menke, D. Borgnia, P. M. Preiss, F. Grusdt, A. M. Kaufman, and M. Greiner, *Nature (London)* **546**, 519 (2017).
- [70] M. P. A. Fisher, P. B. Weichman, G. Grinstein, and D. S. Fisher, *Phys. Rev. B* **40**, 546 (1989).
- [71] D. Jaksch, C. Bruder, J. I. Cirac, C. W. Gardiner, and P. Zoller, *Phys. Rev. Lett.* **81**, 3108 (1998).
- [72] E. Orignac and T. Giamarchi, *Phys. Rev. B* **64**, 144515 (2001).
- [73] D. Hülgel and B. Paredes, *Phys. Rev. A* **89**, 023619 (2014).
- [74] A. Petrescu and K. Le Hur, *Phys. Rev. Lett.* **111**, 150601 (2013).

- [75] M. Piraud, F. Heidrich-Meisner, I. P. McCulloch, S. Greschner, T. Vekua, and U. Schollwöck, *Phys. Rev. B* **91**, 140406(R) (2015).
- [76] A. Dhar, T. Mishra, M. Maji, R. V. Pai, S. Mukerjee, and A. Paramekanti, *Phys. Rev. B* **87**, 174501 (2013).
- [77] S. Greschner, M. Piraud, F. Heidrich-Meisner, I. P. McCulloch, U. Schollwöck, and T. Vekua, *Phys. Rev. Lett.* **115**, 190402 (2015).
- [78] R. B. Laughlin, *Phys. Rev. Lett.* **50**, 1395 (1983).
- [79] E. Cornfeld and E. Sela, *Phys. Rev. B* **92**, 115446 (2015).
- [80] M. Calvanese Strinati, E. Cornfeld, D. Rossini, S. Barbarino, M. Dalmonte, R. Fazio, E. Sela, and L. Mazza, *Phys. Rev. X* **7**, 021033 (2017).
- [81] M. Creutz, *Phys. Rev. Lett.* **83**, 2636 (1999).
- [82] M. Creutz, *Rev. Mod. Phys.* **73**, 119 (2001).
- [83] D. B. Kaplan, *Phys. Lett. B* **288**, 342 (1992).
- [84] K. Jansen and M. Schmaltz, *Phys. Lett. B* **296**, 374 (1992).
- [85] M. F. Golterman, K. Jansen, and D. B. Kaplan, *Phys. Lett. B* **301**, 219 (1993).
- [86] D. B. Kaplan, Chiral symmetry and lattice fermions, Modern Perspectives in Lattice QCD Quantum Field Theory and High Performance Computing, in *Proceedings, International School, 93rd Session* (2009), pp. 223–272.
- [87] J. B. Kogut, *Rev. Mod. Phys.* **51**, 659 (1979).
- [88] J. B. Kogut, *Rev. Mod. Phys.* **55**, 775 (1983).
- [89] D. Leykam, A. Andreanov, and S. Flach, *Adv. Phys.: X* **3**, 1473052 (2018).
- [90] J. Vidal, R. Mosseri, and B. Douçot, *Phys. Rev. Lett.* **81**, 5888 (1998).
- [91] L. Mazza, A. Bermudez, N. Goldman, M. Rizzi, M. A. Martin-Delgado, and M. Lewenstein, *New J. Phys.* **14**, 015007 (2012).
- [92] C. G. Velasco and B. Paredes, [arXiv:1907.11460](https://arxiv.org/abs/1907.11460).
- [93] O. Viyuela, A. Rivas, and M. A. Martin-Delgado, *Phys. Rev. B* **86**, 155140 (2012).
- [94] O. Viyuela, A. Rivas, and M. A. Martin-Delgado, *Phys. Rev. Lett.* **112**, 130401 (2014).
- [95] A. Bermudez, D. Patanè, L. Amico, and M. A. Martin-Delgado, *Phys. Rev. Lett.* **102**, 135702 (2009).
- [96] R. Jafari, H. Johannesson, A. Langari, and M. A. Martin-Delgado, *Phys. Rev. B* **99**, 054302 (2019).
- [97] N. Sun and L.-K. Lim, *Phys. Rev. B* **96**, 035139 (2017).
- [98] S. D. Huber and E. Altman, *Phys. Rev. B* **82**, 184502 (2010).
- [99] S. Takayoshi, H. Katsura, N. Watanabe, and H. Aoki, *Phys. Rev. A* **88**, 063613 (2013).
- [100] M. Tovmasyan, E. P. L. van Nieuwenburg, and S. D. Huber, *Phys. Rev. B* **88**, 220510(R) (2013).
- [101] H. Alaeian, Chung Wai Sandbo Chang, M. V. Moghaddam, C. M. Wilson, E. Solano, and E. Rico, *Phys. Rev. A* **99**, 053834 (2019).
- [102] J. Zurita, C. E. Creffield, and G. Platero, *Adv. Quantum Technol.* **3**, 1900105 (2020).
- [103] Y. He, R. Mao, H. Cai, J.-X. Zhang, Y. Li, L. Yuan, S.-Y. Zhu, and D.-W. Wang, *Phys. Rev. Lett.* **126**, 103601 (2021).
- [104] S. Rachel, *Rep. Prog. Phys.* **81**, 116501 (2018).
- [105] N. B. Kopnin, T. T. Heikkilä, and G. E. Volovik, *Phys. Rev. B* **83**, 220503(R) (2011).
- [106] S. Peotta and P. Törmä, *Nat. Commun.* **6**, 8944 (2015).
- [107] M. Tovmasyan, S. Peotta, P. Törmä, and S. D. Huber, *Phys. Rev. B* **94**, 245149 (2016).
- [108] M. Tovmasyan, S. Peotta, L. Liang, P. Törmä, and S. D. Huber, *Phys. Rev. B* **98**, 134513 (2018).
- [109] R. Mondaini, G. G. Batrouni, and B. Grémaud, *Phys. Rev. B* **98**, 155142 (2018).
- [110] D. Sticlet, L. Seabra, F. Pollmann, and J. Cayssol, *Phys. Rev. B* **89**, 115430 (2014).
- [111] Y. Kuno, T. Orito, and I. Ichinose, *New J. Phys.* **22**, 013032 (2020).
- [112] C. Danieli, A. Andreanov, and S. Flach, *Phys. Rev. B* **102**, 041116(R) (2020).
- [113] R. Nandkishore and D. A. Huse, *Annu. Rev. Condens. Matter Phys.* **6**, 15 (2015).
- [114] O. Boada, A. Celi, J. I. Latorre, and M. Lewenstein, *Phys. Rev. Lett.* **108**, 133001 (2012).
- [115] A. Celi, P. Massignan, J. Ruseckas, N. Goldman, I. B. Spielman, G. Juzeliūnas, and M. Lewenstein, *Phys. Rev. Lett.* **112**, 043001 (2014).
- [116] T. Ozawa and H. M. Price, *Nat. Rev. Phys.* **1**, 349 (2019).
- [117] M. Mancini, G. Pagano, G. Cappellini, L. Livi, M. Rider, J. Catani, C. Sias, P. Zoller, M. Inguscio, M. Dalmonte, and L. Fallani, *Science* **349**, 1510 (2015).
- [118] B. K. Stuhl, H.-I. Lu, L. M. Ayccock, D. Genkina, and I. B. Spielman, *Science* **349**, 1514 (2015).
- [119] J. H. Han, J. H. Kang, and Y. Shin, *Phys. Rev. Lett.* **122**, 065303 (2019).
- [120] L. F. Livi, G. Cappellini, M. Diem, L. Franchi, C. Clivati, M. Frittelli, F. Levi, D. Calonico, J. Catani, M. Inguscio, and L. Fallani, *Phys. Rev. Lett.* **117**, 220401 (2016).
- [121] S. Kolkowitz, S. L. Bromley, T. Bothwell, M. L. Wall, G. E. Marti, A. P. Koller, X. Zhang, A. M. Rey, and J. Ye, *Nature (London)* **542**, 66 (2017).
- [122] S. L. Bromley, S. Kolkowitz, T. Bothwell, D. Kedar, A. Safavi-Naini, M. L. Wall, C. Salomon, A. M. Rey, and J. Ye, *Nat. Phys.* **14**, 399 (2018).
- [123] A. V. Gorshkov, M. Hermele, V. Gurarie, C. Xu, P. S. Julienne, J. Ye, P. Zoller, E. Demler, M. D. Lukin, and A. M. Rey, *Nat. Phys.* **6**, 289 (2010).
- [124] G. Pagano, M. Mancini, G. Cappellini, P. Lombardi, F. Schäfer, H. Hu, X.-J. Liu, J. Catani, C. Sias, M. Inguscio, and L. Fallani, *Nat. Phys.* **10**, 198 (2014).
- [125] S. Barbarino, L. Taddia, D. Rossini, L. Mazza, and R. Fazio, *New J. Phys.* **18**, 035010 (2016).
- [126] T. Bilitewski and N. R. Cooper, *Phys. Rev. A* **94**, 023630 (2016).
- [127] T. Y. Saito and S. Furukawa, *Phys. Rev. A* **95**, 043613 (2017).
- [128] L. Taddia, E. Cornfeld, D. Rossini, L. Mazza, E. Sela, and R. Fazio, *Phys. Rev. Lett.* **118**, 230402 (2017).
- [129] S. Barbarino, M. Dalmonte, R. Fazio, and G. E. Santoro, *Phys. Rev. A* **97**, 013634 (2018).
- [130] M. Calvanese Strinati, S. Sahoo, K. Shtengel, and E. Sela, *Phys. Rev. B* **99**, 245101 (2019).
- [131] J. Jünemann, A. Piga, S.-J. Ran, M. Lewenstein, M. Rizzi, and A. Bermudez, *Phys. Rev. X* **7**, 031057 (2017).
- [132] A. Eckardt, *Rev. Mod. Phys.* **89**, 011004 (2017).
- [133] J. Zak, *Phys. Rev. Lett.* **62**, 2747 (1989).
- [134] M. V. Berry, *Proc. R. Soc. London A* **392**, 45 (1984).
- [135] A. P. Schnyder, S. Ryu, A. Furusaki, and A. W. W. Ludwig, *Phys. Rev. B* **78**, 195125 (2008).
- [136] A. Kitaev, *AIP Conf. Proc.* **1134**, 22 (2009).

- [137] S. A. Parameswaran, R. Roy, and S. L. Sondhi, *C. R. Phys.* **14**, 816 (2013).
- [138] K. G. Wilson, in *New Phenomena in Subnuclear Physics* (Springer New York, London, 1977), pp. 69–142.
- [139] D. J. Gross and A. Neveu, *Phys. Rev. D* **10**, 3235 (1974).
- [140] E. Fermi, *Z. Phys.* **88**, 161 (1934).
- [141] F. L. Wilson, *Am. J. Phys.* **36**, 1150 (1968).
- [142] A. Bermudez, E. Tirrito, M. Rizzi, M. Lewenstein, and S. Hands, *Ann. Phys.* **399**, 149 (2018).
- [143] E. Tirrito, M. Rizzi, G. Sierra, M. Lewenstein, and A. Bermudez, *Phys. Rev. B* **99**, 125106 (2019).
- [144] A. Hamed Moosavian and S. Jordan, *Phys. Rev. A* **98**, 012332 (2018).
- [145] D.-S. Li, H. Wang, C. Guo, M. Zhong, and P.-X. Chen, *arXiv:2011.07538*.
- [146] A. M. Czajka, Z.-B. Kang, H. Ma, and F. Zhao, *arXiv:2112.03944*.
- [147] S. Aoki, *Phys. Rev. D* **30**, 2653 (1984).
- [148] S. Sharpe and R. Singleton, *Phys. Rev. D* **58**, 074501 (1998).
- [149] D. B. Kaplan, *arXiv:0912.2560*.
- [150] W. Sun, B.-Z. Wang, X.-T. Xu, C.-R. Yi, L. Zhang, Z. Wu, Y. Deng, X.-J. Liu, S. Chen, and J.-W. Pan, *Phys. Rev. Lett.* **121**, 150401 (2018).
- [151] B. Song, L. Zhang, C. He, T. F. J. Poon, E. Hajiyev, S. Zhang, X.-J. Liu, and G.-B. Jo, *Sci. Adv.* **4**, eaao4748 (2018).
- [152] Z. Wu, L. Zhang, W. Sun, X.-T. Xu, B.-Z. Wang, S.-C. Ji, Y. Deng, S. Chen, X.-J. Liu, and J.-W. Pan, *Science* **354**, 83 (2016).
- [153] M.-C. Liang, Y.-D. Wei, L. Zhang, X.-J. Wang, H. Zhang, W.-W. Wang, W. Qi, X.-J. Liu, and X. Zhang, *arXiv:2109.08885*.
- [154] H. Nielsen and M. Ninomiya, *Nucl. Phys. B* **185**, 20 (1981).
- [155] H. Nielsen and M. Ninomiya, *Nucl. Phys. B* **193**, 173 (1981).
- [156] N. Manton, *Ann. Phys.* **159**, 220 (1985).
- [157] J. Ambjørn, J. Greensite, and C. Peterson, *Nucl. Phys. B* **221**, 381 (1983).
- [158] L. Fu, *Phys. Rev. Lett.* **106**, 106802 (2011).
- [159] Y. Ando and L. Fu, *Annu. Rev. Condens. Matter Phys.* **6**, 361 (2015).
- [160] H. Isobe and L. Fu, *Phys. Rev. B* **92**, 081304(R) (2015).
- [161] E. Lieb, T. Schultz, and D. Mattis, *Ann. Phys.* **16**, 407 (1961).
- [162] E. Barouch and B. M. McCoy, *Phys. Rev. A* **3**, 786 (1971).
- [163] T. Moriya, *Phys. Rev.* **120**, 91 (1960).
- [164] I. Dzyaloshinsky, *J. Phys. Chem. Solids* **4**, 241 (1958).
- [165] P. Jordan and E. Wigner, *Z. Phys.* **47**, 631 (1928).
- [166] N. N. Bogoljubov, *Il Nuovo Cimento* **7**, 794 (1958).
- [167] H. Bruus and K. Flensberg, *Many-Body Quantum Theory in Condensed Matter Physics: An Introduction* (Oxford University Press, Oxford, 2017).
- [168] P. Coleman, *Introduction to Many-Body Physics* (Cambridge University Press, Cambridge, 2015).
- [169] M. C. Bañuls and K. Cichy, *Rep. Prog. Phys.* **83**, 024401 (2020).
- [170] F. Pollmann, A. M. Turner, E. Berg, and M. Oshikawa, *Phys. Rev. B* **81**, 064439 (2010).
- [171] A. Dhar, M. Maji, T. Mishra, R. V. Pai, S. Mukerjee, and A. Paramekanti, *Phys. Rev. A* **85**, 041602(R) (2012).
- [172] A. Tokuno and A. Georges, *New J. Phys.* **16**, 073005 (2014).
- [173] M. P. Zaletel, S. A. Parameswaran, A. Rüegg, and E. Altman, *Phys. Rev. B* **89**, 155142 (2014).
- [174] V. Aji and C. M. Varma, *Phys. Rev. B* **75**, 224511 (2007).
- [175] V. Chua, H. Yao, and G. A. Fiete, *Phys. Rev. B* **83**, 180412(R) (2011).
- [176] L. Messio, B. Bernu, and C. Lhuillier, *Phys. Rev. Lett.* **108**, 207204 (2012).
- [177] S. Yan, D. A. Huse, and S. R. White, *Science* **332**, 1173 (2011).
- [178] D. Hueriga, J. Dukelsky, N. Laflorencie, and G. Ortiz, *Phys. Rev. B* **89**, 094401 (2014).
- [179] M. B. Plenio and S. S. Virmani, *Quant. Inform. Coherence*, 173 (2014).
- [180] L. Amico, R. Fazio, A. Osterloh, and V. Vedral, *Rev. Mod. Phys.* **80**, 517 (2008).
- [181] H. Li and F. D. M. Haldane, *Phys. Rev. Lett.* **101**, 010504 (2008).
- [182] L. Fidkowski, *Phys. Rev. Lett.* **104**, 130502 (2010).
- [183] F. Pollmann, E. Berg, A. M. Turner, and M. Oshikawa, *Phys. Rev. B* **85**, 075125 (2012).
- [184] G. Vidal, J. I. Latorre, E. Rico, and A. Kitaev, *Phys. Rev. Lett.* **90**, 227902 (2003).
- [185] P. Calabrese and J. Cardy, *J. Stat. Mech.* (2004) P06002.
- [186] P. Calabrese and J. Cardy, *J. Phys. A: Math. Theor.* **42**, 504005 (2009).
- [187] I. Bloch, J. Dalibard, and W. Zwerger, *Rev. Mod. Phys.* **80**, 885 (2008).
- [188] J. H. Kang, J. H. Han, and Y. Shin, *Phys. Rev. Lett.* **121**, 150403 (2018).
- [189] J. H. Kang, J. H. Han, and Y. Shin, *New J. Phys.* **22**, 013023 (2020).
- [190] W. Hofstetter, J. I. Cirac, P. Zoller, E. Demler, and M. D. Lukin, *Phys. Rev. Lett.* **89**, 220407 (2002).
- [191] D. Jaksch and P. Zoller, *New J. Phys.* **5**, 56 (2003).
- [192] M. Reitter, J. Näger, K. Wintersperger, C. Sträter, I. Bloch, A. Eckardt, and U. Schneider, *Phys. Rev. Lett.* **119**, 200402 (2017).
- [193] K. Wintersperger, M. Bukov, J. Näger, S. Lellouch, E. Demler, U. Schneider, I. Bloch, N. Goldman, and M. Aidelsburger, *Phys. Rev. X* **10**, 011030 (2020).
- [194] W. Xu, W. Morong, H.-Y. Hui, V. W. Scarola, and B. DeMarco, *Phys. Rev. A* **98**, 023623 (2018).
- [195] M. Messer, K. Sandholzer, F. Görg, J. Minguzzi, R. Desbuquois, and T. Esslinger, *Phys. Rev. Lett.* **121**, 233603 (2018).
- [196] F. Görg, K. Sandholzer, J. Minguzzi, R. Desbuquois, M. Messer, and T. Esslinger, *Nat. Phys.* **15**, 1161 (2019).
- [197] K. Viebahn, J. Minguzzi, K. Sandholzer, A.-S. Walter, M. Sajnani, F. Görg, and T. Esslinger, *Phys. Rev. X* **11**, 011057 (2021).
- [198] X.-J. Liu, Z.-X. Liu, and M. Cheng, *Phys. Rev. Lett.* **110**, 076401 (2013).
- [199] X.-J. Liu, K. T. Law, and T. K. Ng, *Phys. Rev. Lett.* **112**, 086401 (2014).
- [200] X.-J. Liu, K. T. Law, and T. K. Ng, *Phys. Rev. Lett.* **113**, 059901(E) (2014).
- [201] L. Ziegler, E. Tirrito, M. Lewenstein, S. Hands, and A. Bermudez, *arXiv:2011.08744*.
- [202] L. Ziegler, E. Tirrito, M. Lewenstein, S. Hands, and A. Bermudez, *arXiv:2111.04485*.

- [203] F. Gerbier and J. Dalibard, *New J. Phys.* **12**, 033007 (2010).
- [204] N. Q. Burdick, Y. Tang, and B. L. Lev, *Phys. Rev. X* **6**, 031022 (2016).
- [205] B. Song, C. He, S. Zhang, E. Hajiyevev, W. Huang, X.-J. Liu, and G.-B. Jo, *Phys. Rev. A* **94**, 061604(R) (2016).
- [206] D. González-Cuadra, L. Tagliacozzo, M. Lewenstein, and A. Bermudez, *Phys. Rev. X* **10**, 041007 (2020).
- [207] G. Magnifico, D. Vodola, E. Ercolessi, S. P. Kumar, M. Müller, and A. Bermudez, *Phys. Rev. D* **99**, 014503 (2019).
- [208] G. Magnifico, D. Vodola, E. Ercolessi, S. P. Kumar, M. Müller, and A. Bermudez, *Phys. Rev. B* **100**, 115152 (2019).
- [209] P. Jordan and E. P. Wigner, in *The Collected Works of Eugene Paul Wigner* (Springer, Heidelberg, 1993), pp. 109–129.